CHAPTER 1

Overview of sea ice growth and properties

Chris Petrich[1] and Hajo Eicken[2]

[1] *Northern Research Institute Narvik, Narvik, Norway*
[2] *University of Alaska Fairbanks, Fairbanks, AK, USA*

1.1 Introduction

A recent, substantial reduction in summer Arctic sea ice extent and its potential ecological and geopolitical impacts generated a lot of attention in the media and among the general public. The satellite remote-sensing data documenting such recent changes in ice coverage are collected at coarse spatial scales (Chapter 9) and typically cannot resolve details finer than about 10 km in lateral extent. However, many of the processes that make sea ice such an important aspect of the polar oceans occur at much smaller scales, ranging from the sub-millimetre to the metre scale. An understanding of how large-scale behaviour of sea ice monitored by satellite relates to and depends on the processes driving ice growth and decay requires an understanding of the evolution of ice structure and properties at these finer scales and this is the subject of this chapter.

The macroscopic properties of sea ice are of interest in many practical applications discussed in this book. They are derived from microscopic properties as continuum properties averaged over a specific volume (representative elementary volume) or mass of sea ice. This is not unlike macroscopic temperature and can be derived from microscopic molecular movement. The macroscopic properties of sea ice are determined by the microscopic structure of the ice, i.e. the distribution, size and morphology of ice crystals and inclusions. The challenge is to see both the forest (i.e. the role of sea ice in the environment) and the trees (i.e. the way in which the constituents of sea ice control key properties and processes). In order to understand and project how the forest will respond to changes in its environment, we have to understand the life cycle of its constituents, the trees. Here, we will adopt a bottom-up approach, starting with the trees, characterizing microscopic properties and processes and how they determine macroscopic properties, to lay the groundwork for understanding the forest. In using this approach, we will build up from the sub-millimetre scale and conclude with the larger scales shown in Figure 1.1.

Sea ice would not be sea ice without salt. In fact, take away the salt and we are left with lake ice, differing in almost all aspects that we discuss in this chapter. The microscopic and macroscopic redistribution of ions opens the path to understanding all other macroscopic properties of sea ice. We will therefore start in Section 1.2 by looking at the influence of ions on ice growth at the scale of individual ice crystals, in sea ice growing under both rough and quiescent conditions. We will continue in Section 1.3 by looking at the dynamic feedback system between fluid dynamics and pore volume, both microscopically and at the continuum scale. We will point out that our knowledge is far from exhaustive in this fundamental aspect. However, armed with a basic understanding of crystal structure, phase equilibria and pore structure, we can shed light on ice optical, dielectric and thermal properties and macroscopic ice strength in Section 1.4. One of the most discussed aspects of sea ice is its presence or absence. We will look at the growth and energy budget of sea ice and touch on deformation and decay processes in Section 1.5.

1.1.1 Lake ice versus sea ice

Ice in a small lake tends to form before coastal sea ice at a similar location. This is largely explained by the fact that,

I. Ice growth

Agitated conditions

Calm conditions

Ice growth through quiescent bottom freezing

Grease ice: aggregations of frazil (spuicles and platelets of ice) into surface layer

Nilas:
• dark nilas (<5 cm thick)
• light nilas (5–10 cm thick)

First-year white ice

Ice growth in a wave-field

Pancake ice: consolidation of frazil into larger units

Young ice:
• grey ice (0.1–0.15 m)
• grey-white ice (0.15–0.3 m)

Old ice (second- and multi-years)

II. Ice deformation

Convergent regimes

Divergent regimes

Rafting (mostly confined to thin ice)

Ridging

Crack

Lead

III. Ice evolution and melting

Snow deposition and flooding

Melting

Depression of surface below sealevel

Complete melting of floes

Snow deposition

Surface melt puddles

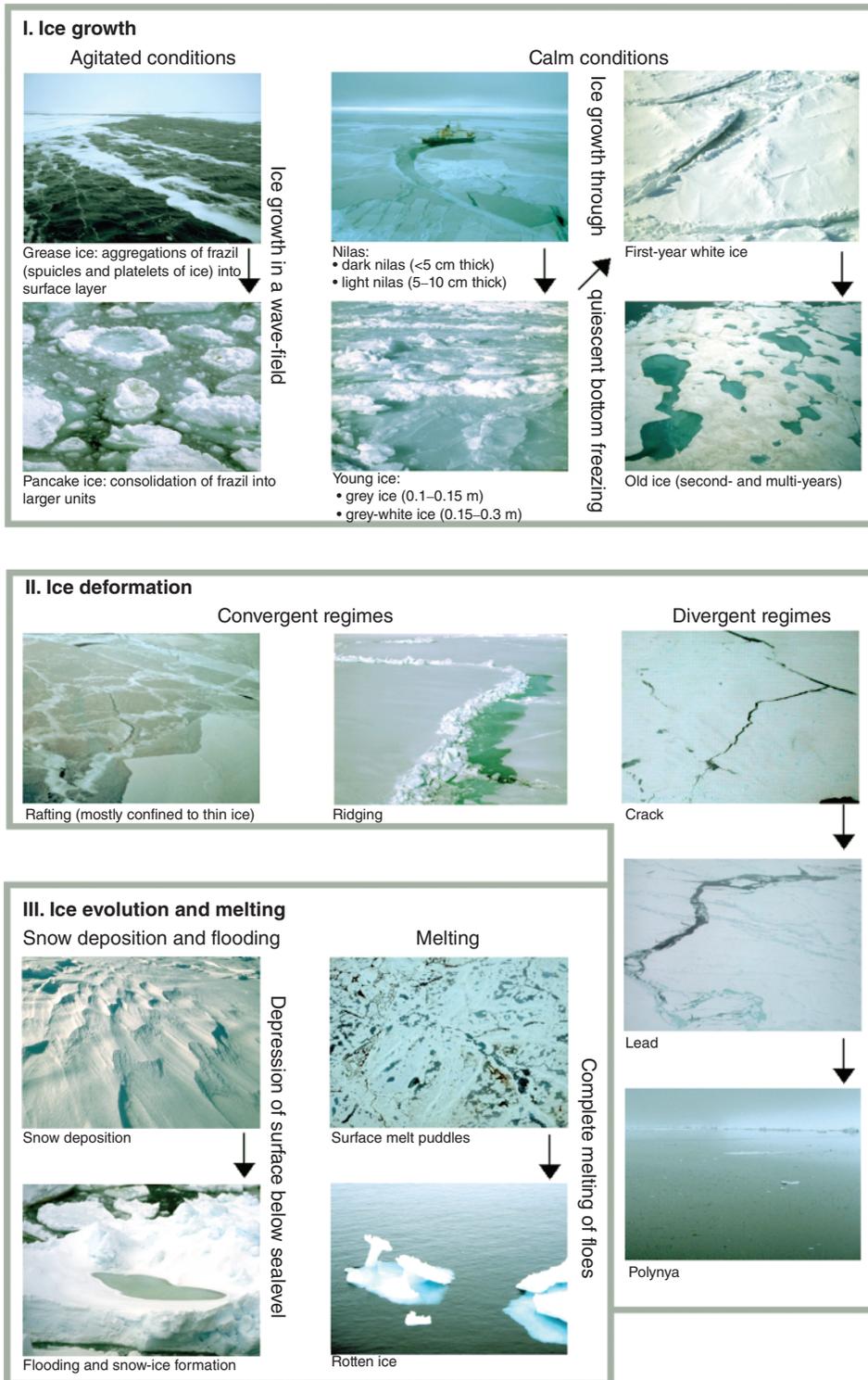Flooding and snow-ice formation

Rotten ice

Polynya

Figure 1.1 Ice types, pack ice features and growth, melt and deformation processes.

in contrast to freshwater, the temperature of maximum density of seawater is not above the freezing point. If a freshwater body is cooled from above then the water body undergoes convective overturning until the temperature reaches +4°C, after which the coldest water stays at the surface where it is cooled rapidly. Hence, ice formation starts relatively early in the season but progresses slowly as the underlying water mass is still above freezing. The situation is different if strong winds continuously overturn the water (e.g. in big lakes), or if ice grows from seawater. In these cases, the entire mixed layer has to be cooled to the freezing point before ice formation sets in. Once this happens, however, thickening progresses relatively quickly.

Salt further impacts ice microstructure. The photographs in Figure 1.2 show the surface of snow-free lake ice and sea ice in spring near Barrow, Alaska. Despite comparable thickness and growth conditions,

lake ice, transparent, appears much darker than sea ice, which scatters light. This is also expressed in a large difference in albedo (the fraction of the incident short-wave radiation reflected from a surface; Section 1.4), such that more than three-quarters of the incoming short-wave irradiative flux penetrates the lake ice surface into the underlying water, compared with less than half for a sea ice cover. This has substantial consequences for the heat budget of the ice cover and the water beneath. The fact that sea ice albedo is typically higher than open water albedo by a factor of up to 10 gives rise to the so-called ice–albedo feedback: a perturbation in the surface energy balance resulting in a decreased sea ice extent due to warming may amplify, as the ice cover reduction increases the amount of solar energy absorbed by the system (Chapter 4; Curry et al., 1995; Perovich et al., 2007). For low-albedo lake ice, this effect is less pronounced. What causes these
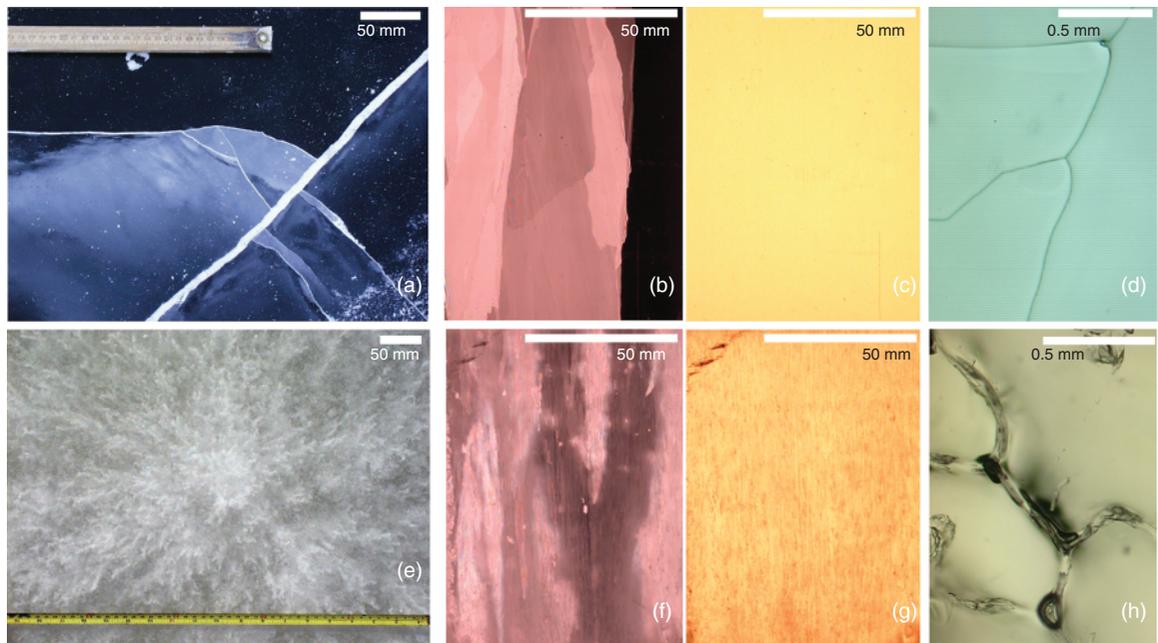
Figure 1.2 Surface appearance and microstructure of winter lake ice (Imikpuk Lake, top, panels a–d) and sea ice (Chukchi Sea landfast ice, bottom, panels e–h) near Barrow, Alaska. The bright features apparent in the lake ice are cracks that penetrate all the way to the bottom of the ice cover (close to 1 m thick), while the clear, uncracked ice appears completely black (a, top). (e) The sea ice surface photograph shows a network of brine channels that join into a few feeder channels. (b, c, f, g) Photographs of vertical thin sections from the two ice covers, with (b) and (f) recorded between crossed polarizers, highlighting different ice crystals in different colours. Panels (c) and (g) show the same section as (b) and (f) in plain transmitted light, demonstrating the effect of brine inclusions on transparency of the ice. (d, h) Photomicrographs showing the typical pore structure at a temperature of −5°C (lake ice) and −15°C (sea ice), with few thin inclusions along grain boundaries in lake ice (d) and a network of thicker brine inclusions in sea ice (h).

contrasts? As the thin-section photographs in Figure 1.2 demonstrate, lake ice is nearly devoid of millimetre and sub-millimetre liquid inclusions, whereas sea ice can contain more than $10\,mm^{-3}$. The inclusions scatter light due to a contrast in refractive index (Section 1.4). This explains both the high albedo and lack of transparency of thicker sea ice samples.

The crystal microstructure differs between lake ice and sea ice. Lake ice grows with a planar liquid–solid interface rather than a lamellar interface, as is the case of sea ice. In sea ice, brine is trapped between the lamellae at the bottom of the ice, allowing for retention of between 10% and 40% of the ions between the ice crystals. While the differences in bulk ice properties, such as albedo and optical extinction coefficient, are immediately obvious from these images, the physical features and processes responsible for these differences only reveal themselves in the microscopic approach, as exemplified by the thin-section images depicting individual inclusions (Figure 1.2). In the sections that follow, we will consider in more detail how microstructure and microphysics are linked to sea ice growth and evolution, and how both in turn determine the properties of the ice cover as a whole.

1.2   Ions in the water: sea ice microstructure and phase diagram

1.2.1   Crystal structure of ice Ih

The characteristic properties of sea ice and its role in the environment are governed by the crystal lattice structure of ice Ih, in particular its resistance to the incorporation of sea salt ions. Depending on pressure and temperature, water ice can appear in more than 15 different modifications. At the Earth's surface, freezing of water under equilibrium conditions results in the formation of the modification ice Ih, with the 'h' indicating crystal symmetry in the hexagonal system. Throughout this chapter, the term 'ice' refers to ice Ih.

Water molecules (H_2O) in ice are arranged tetrahedrally around each other, with a six-fold rotational symmetry apparent in the so-called basal plane (Figure 1.3). This is why snowflakes have six-fold symmetry. The principal crystallographic axis [referred to either as the corresponding unit vector (0001) or simply as the c-axis] is normal to the basal plane and corresponds to the axis of maximum rotational symmetry (Figure 1.3). The interface of the basal plane is smooth at the molecular level. The basal plane is spanned by the crystal a-axes, and the crystal faces
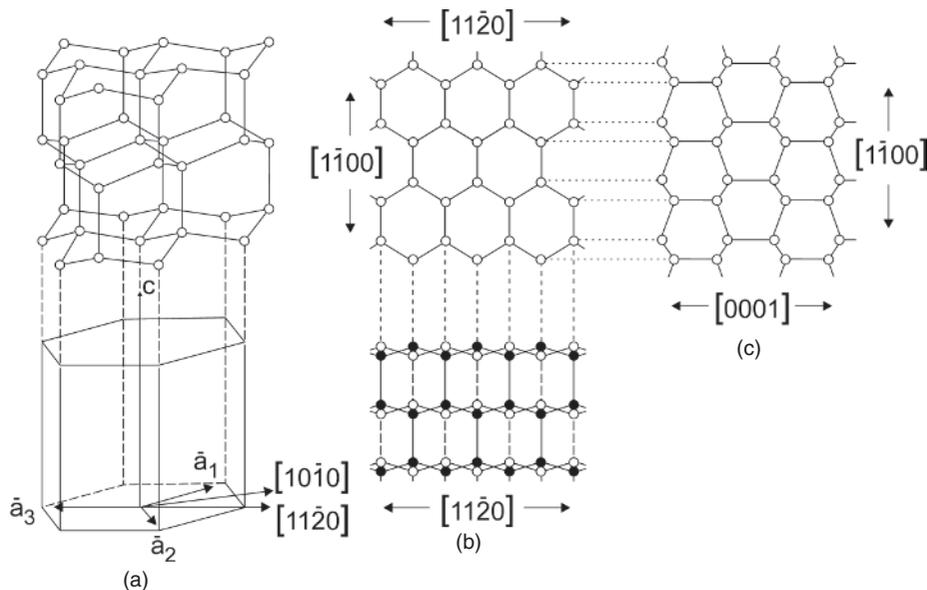
Figure 1.3 Crystal structure of ice Ih (from Weeks & Ackley, 1986). The c-axis is indicated at left and right, and the centre panels correspond to a view along (top) and normal (bottom) to the c-axis.

perpendicular to this plane are rough at the molecular level. The different interface morphologies result in different interface kinetics and are responsible for a pronounced anisotropy in growth rates. For example, the higher growth rates in the basal plane lead to the development of individual frazil ice crystals with thickness-to-width ratios on the order of 1:10 to 1:100 (Hobbs, 1974). Another key aspect of the ice crystal structure is the fact that the packing density of water molecules in ice, and hence its material density, is lower than in the liquid. In the liquid state, water molecules are arranged as hydrate shells surrounding impurities (e.g. sea salt ions) owing to the strong polarity of the water molecule. However, accommodation of sea salt ions is greatly restricted in the ice crystal lattice. Only very few species of ions and molecules are incorporated in the ice crystal lattice in appreciable quantities (either replacing water molecules or filling voids) owing to constraints on size and electric charge. Among them are fluorine and ammonium ions and some gases. However, the major ions present in seawater (Na^+, K^+, Ca^{2+}, Mg^{2+}, Cl^-, SO_4^{2-}, CO_3^{2-}) are not incorporated into the ice crystal lattice, are rejected from the crystal and accumulate at the interface during crystal growth. This has important consequences for the microstructure and properties of sea ice, as part of the salt is retained in liquid inclusions between the ice lamellae, while a larger fraction eventually enters the underlying water column. Both of these processes and their implications will be discussed in the following subsections and in Sections 1.3 and 1.4.

1.2.2 Columnar ice microstructure and texture

As ice grows and the ice–water interface advances downwards into the melt, ions are rejected from the ice. The solute concentration of ions builds up ahead of the advancing interface, increasing the salinity of a thin layer of a few millimetres in thickness. The resulting gradient in salt concentration leads to diffusion of salt away from the interface towards the less saline ocean. Thermodynamic equilibrium dictates that the microscopic ice–water interface itself is at the respective melting/freezing point. As the freezing point decreases with increasing salinity, an increase in salt concentration goes along with a drop in temperature. This leads to a heat flux from the ocean towards the now colder interface.

Heat transport through this boundary layer from the warmer ocean to the colder interface is faster than ion diffusion away from the enriched interface. As a result, a thin layer is established ahead of the interface that is cooled below the freezing point of the ocean but only slightly enriched in salinity above the ocean level. This layer is said to be constitutionally super-cooled as its temperature is below the freezing point of the brine (Figure 1.4).

It is this constitutional super-cooling that distinguishes the growth of lake ice from that of sea ice and helps to explain their respective crystallographic properties. Any small (sub-millimetre) perturbation of a planar ice–water interface that protrudes into the constitutionally super-cooled zone finds itself at a growth advantage, as not only is heat conducted upwards and away from the ice–water interface, but the super-cooled water layer also provides a heat sink. Considering that ice grows fastest in the basal plane, crystals with horizontal c-axes quickly outgrow crystals with c-axes off the horizontal in a process termed geometric selection. By the time ice is thicker than 0.2 m, the c-axes of the remaining crystals are almost exclusively horizontal (Weeks & Wettlaufer, 1996). The solute rejected by a protrusion contributes to a freezing point reduction of the brine along the protrusion boundaries. Consequently, such perturbations can grow into ordered patterns of lamellar bulges at the ice–water interface (for a quantitative analysis of constitutional super-cooling, see Weeks, 2010). The morphology of the interface is mostly reported to be lamellar or cellular (Figure 1.5). In the case of brackish ice grown from
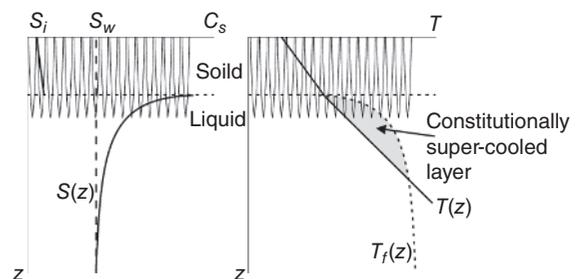
Figure 1.4 Schematic depiction of the lamellar ice–water interface (skeletal layer) and the corresponding salinity (left) and temperature (right) gradients. The freezing temperature profile is shown as a dashed line at right, with a constitutionally super-cooled layer bounded by the actual temperature gradient and the salinity-dependent freezing-point curve.
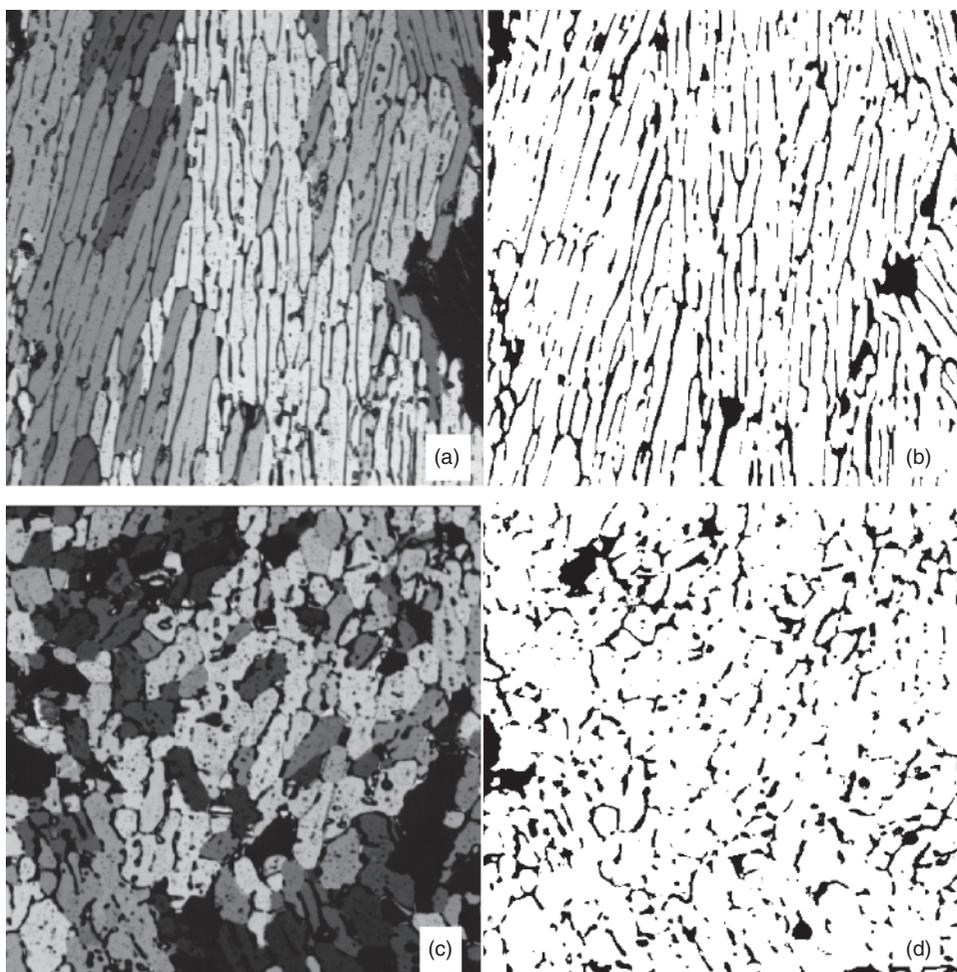
Figure 1.5 (a–d) Thin-section photographs of columnar sea ice grown in a large ice tank (Hamburg Environmental Test Basin, INTERICE experiments) in the absence of an under-ice current (a, b; porosity 0.154, mean pore area 0.096 mm^2) and with a current speed of 0.16 m s^{-1} (c, d; porosity 0.138, mean pore area 0.077 mm^2). Images (a) and (c) have been recorded between crossed polarizers (section is 20 mm wide), with grain boundaries apparent as transitions in grey shades due to different interference colours. Images (b) and (d) show the same section with pores indicated in black based on processing of images recorded in incident light.

water with very low salinities, a planar interface may remain stable throughout the growth process (Weeks & Wettlaufer, 1996).

The growth of individual ice platelets into super-cooled water is most readily observed in the vicinity of Antarctic ice shelves (Jeffries et al., 1993; Leonard et al., 2006) and under Arctic sea ice that is separated from the ocean by a meltwater lens (Notz et al., 2003). Characteristic of the resulting crystal fabric are comparatively large platelets whose *c*-axes deviate from the horizontal seemingly at random. The process of their

formation is poorly understood; one hypothesis is that they are seeded by frazil crystals that formed in the super-cooled water.

When fully developed, as in the case of ordinary columnar sea ice (Figure 1.6), the lamellar interface consists of sub-millimetre-thick blades of ice, separated by narrow films of brine, so-called brine layers. The skeletal layer forms the bottom-most centimetres of sea ice where these brine layers separate individual ice lamellae. It has no appreciable mechanical strength and a porosity of about 30% in its upper reaches. Significant
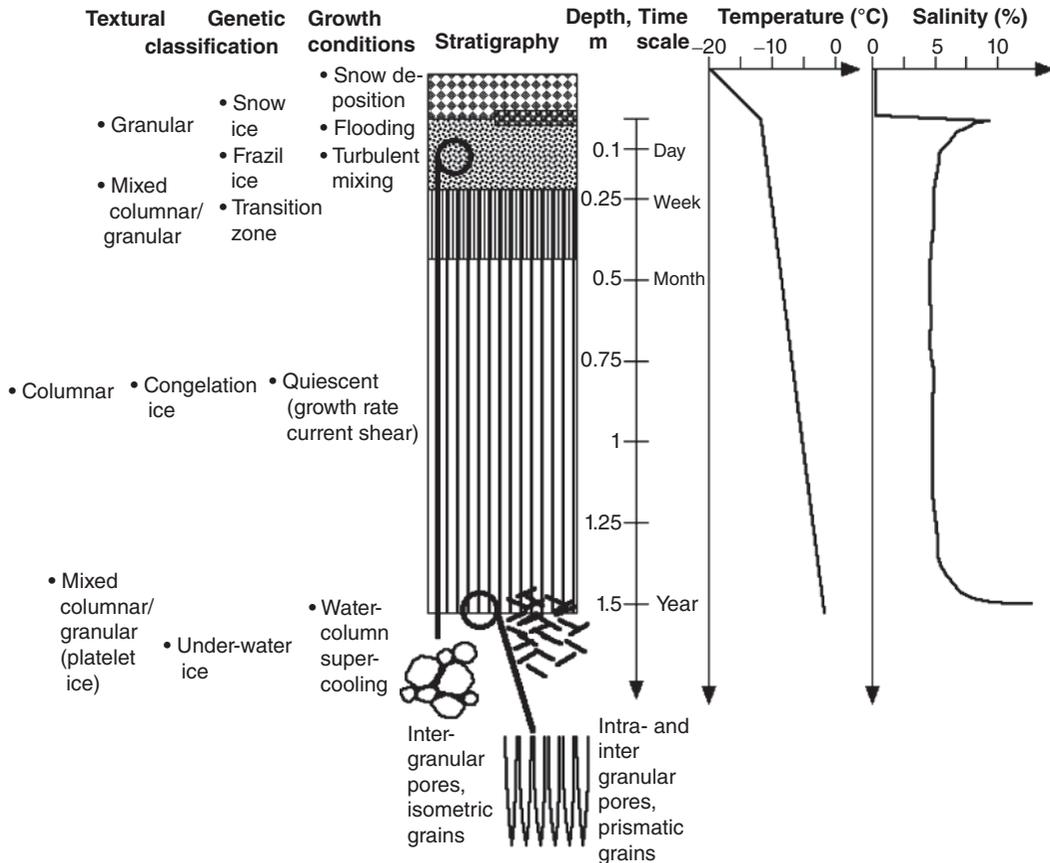
Figure 1.6 Schematic summarizing the main ice textures, growth conditions and timescales and typical winter temperature and salinity profiles for first-year sea ice.

advective brine exchange with the ocean occurs in the skeletal layer and above (Section 1.3).

Consolidation of the skeletal layer follows a trajectory in the phase diagram (Figure 1.7 – although for a smaller bulk salinity than shown in the figure). As the thickness of the ice cover increases, isotherms move downward and the temperature at a given vertical level decreases, ice forms by thickening the lamellae and the fraction of liquid decreases. Eventually, the ice lamellae connect and consolidate into a porous sea ice matrix of strength. During this consolidation process, brine is lost from the ice, as described in more detail in Section 1.3. Although not rigorously accurate, the principal process is the reverse of the warming sequence depicted in Figure 1.8.

The basic crystal pattern laid down in the skeletal layer is retained during ice growth in the form of grain and pore microstructure, i.e. the size and orientation of crystals and the layer spacing of pores. This is illustrated in Figure 1.5, which shows horizontal thin sections of two different varieties of columnar ice grown under the same conditions, except for a difference in the under-ice current. Ice grown in the absence of externally imposed currents exhibits the typical lamellar substructure, with parallel brine layers within individual crystals (also called 'grains'). Along grain boundaries, the size and shape of pores are more heterogeneous, with brine tubes and channels of several millimetres in diameter apparent in the lower right of Figure 1.5(b). The arrangement, shape and size of crystals define the texture of the ice (Figure 1.6).

Ice grown in a current also exhibits a grain substructure delineated by pores, but the degree of parallel alignment of pores and the aspect ratios of individual
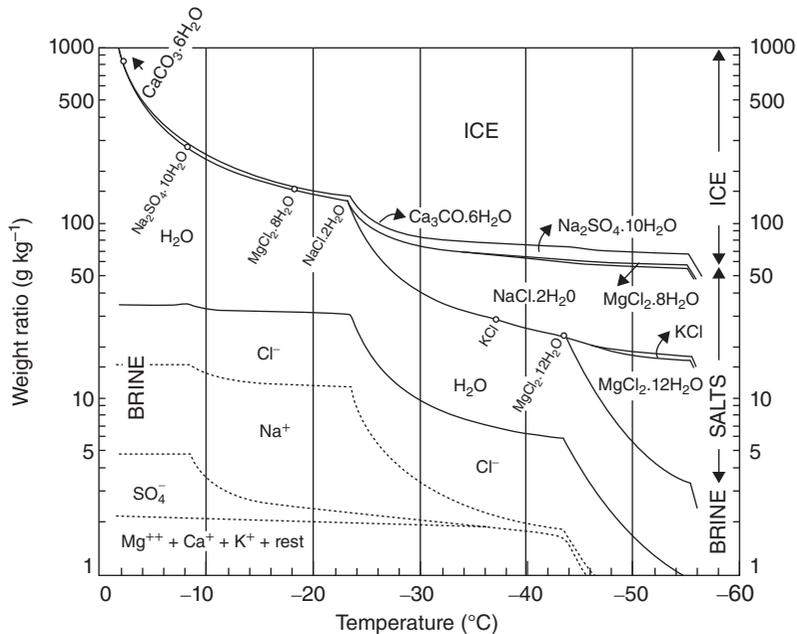
Figure 1.7 Phase diagram of sea ice from Assur (1960). The different curves indicate the mass fraction of solid ice (top), salts (middle) and liquid brine (bottom) present in a closed volume of standard seawater at different temperatures.

inclusions are very different, as are the grain sizes (Figure 1.5c,d). This difference arises from differences in the thickness and degree of super-cooling at the interface, which depend on ice growth rate, seawater salinity and, as illustrated here, the magnitude of currents transporting solute away from the ice. Currents also affect the horizontal orientation of the crystal c-axes.

c-axes tend to point parallel to the direction of a unidirectional under-ice current. It appears that salt transport away from the interface is enhanced for crystals with lamellae oriented perpendicular (c-axes parallel) to the current, providing them with a growth advantage that eventually results in the dominance of c-axes parallel to the current (Langhorne & Robinson, 1986). Hence, under-ice currents enhance the anisotropy of the columnar sea ice.

A further aspect of the lamellar substructure is that the spacing of ice lamellae depends on growth rate. Nakawo & Sinha (1984) demonstrated this for Arctic sea ice, where the down-core reduction in growth rate (see Section 1.5) closely corresponded to an increase in the brine layer spacing a_0. Typically, a_0 is on the order of a few tenths of a millimetre. However, in what is probably the oldest sea ice sampled to date, grown at

rates of a few centimetres per year, Zotikov et al. (1980) found brine layer spacings of several millimetres.

The skeletal layer harbours one of the greatest concentrations of phytoplankton in the world's oceans by providing a habitat for diatoms and other microorganisms and, in turn, grazers (Smith et al., 1990; see also Chapters 13–16). As algae depend not only on sunlight but also on nutrients for photosynthetic activity, in many areas the most active layer of ice organisms is found within the bottom few centimetres of the ice cover, where high porosities and permeabilities and the proximity of the ocean reservoir provide a sufficient influx of inorganic nutrients and gas exchange (Chapters 14, 17 and 18). At the same time, this layer offers some protection from the largest grazers (Chapter 16) and presents photosynthetic organisms with a foothold at the top of the water column where irradiative fluxes are highest (Chapter 14; Eicken, 1992a).

1.2.3 Granular ice microstructure and texture

Water at temperatures below the freezing point is called super-cooled. Typically, seawater cannot be
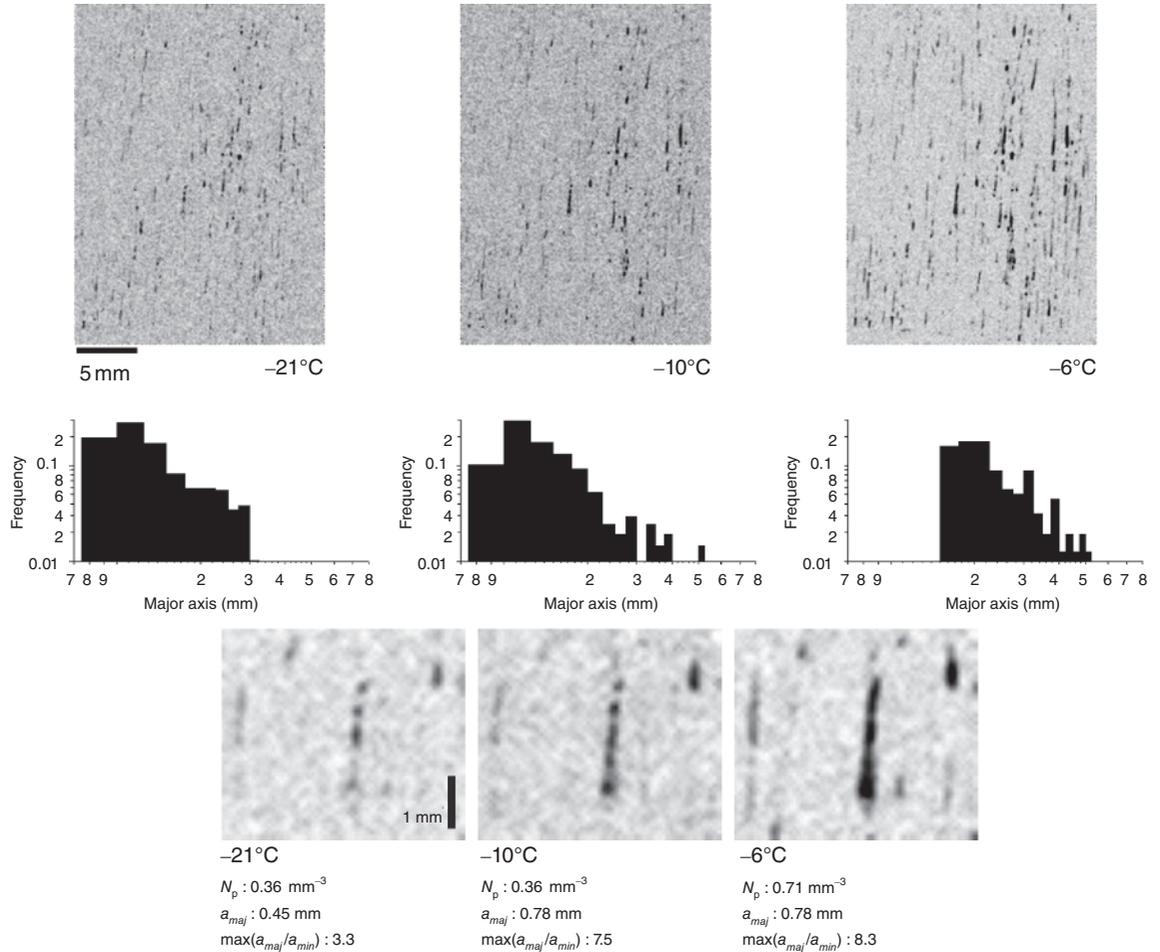
Figure 1.8 Thermal evolution of fluid inclusions in first-year sea ice obtained near Barrow, Alaska (0.13–0.16 m depth, sample obtained in March 1999 and maintained at *in situ* temperatures after sampling up until experiment; for details see Eicken et al., 2000) as studied with magnetic resonance imaging techniques. The upper three panels show a vertical cross-section through the sample as it is warmed, with pores appearing dark. The middle panels show the size distribution of the major pore axes a_{maj} (upper 10th percentile), indicating enlarging and merging of pores in the vertical. The change in pore size, morphology [as indicated by the maximum ratio between major and minor pore axis length, $\max(a_{maj}/a_{min})$] and number density N_p is apparent in the lower panels, which show a smaller subset of pores at 0.15 m depth.

super-cooled by more than 0.1 K because abundant impurities act as nucleation sites for ice crystals (Fletcher, 1970). As a result, ice forming in water subjected to overturning by winds will develop ice crystals that are kept in suspension until a surface layer of ice slush builds up that reduces mixing agitated by wind. These ice crystals take the shape of needles, spicules or platelets, often intertwined into aggregates, and are known as frazil ice (Figure 1.6). Individual crystals are typically a few to a few tens of millimetres in diameter

and less than a millimetre in thickness (Weeks, 2010). The surface slush starts to consolidate by freezing of the interstitial brine from the top downwards. Shielded from winds, the ice grows below the slush in a radically different, quiescent environment.

The stratigraphy of a 'typical' ice cover is revealed through analysis of vertical core sections. It consists of a sequence of granular ice (a few centimetres to tens of centimetres at most in the Arctic, but substantially more in other, more dynamic environments such as

the Antarctic), with randomly oriented, isomeric or prismatic crystals [see detailed descriptions in Weeks (2010) and Tyshko et al. (1997)], followed by a transitional layer that is underlain by columnar ice (congelation ice), composed of vertically elongated prismatic crystals that can grow to several centimetres in diameter and tens of centimetres in length (Figure 1.6; see above for details).

1.2.4   Frazil ice

Congelation growth of sea ice with columnar texture typically dominates in the Arctic. However, frazil ice growth resulting in granular textures is also common and even more so in the Southern Ocean. Growth of individual platelets and needles of frazil in a super-cooled water column differs from growth of congelation ice insofar as both heat and salt have to be transported away from the interface into the surrounding ocean water. Consequently, beyond a certain size, individual frazil crystals develop rough, dendritic surfaces as a result of solute build-up. Frazil growing in the turbulent uppermost metres of the ocean has the tendency to aggregate into clusters of crystals. The clusters are capable of sweeping particulates and biota from the water column, and carrying them to the surface as a layer of frazil or grease ice accumulates (Reimnitz et al., 1990; Smedsrud, 2001; Chapter 7). Despite its abundance, some aspects of frazil growth are not that well understood: its inherent 'stickiness', enhancing concentrations of biota in Antarctic sea ice, or the conditions governing the growth of larger ice platelets at greater depths (Bombosch, 1998). Frazil ice growth in the presence of melting Antarctic ice shelves is capable of generating large volumes of crystals that contribute to the mass balance of both ice shelves and coastal sea ice (e.g. Leonard et al., 2006).

Another aspect of frazil growth that is currently not well understood is the actual consolidation of loose masses of frazil crystals, with ice volume fractions of between about 10% and 30% in solid granular sea ice. Evidence from oxygen stable-isotope and salinity measurements of individual crystals and layers of granular ice suggests that the consolidation process is a combination of downward freezing of voids among the mesh of frazil crystals and transformations in the size distribution and morphology of the crystals themselves. This is similar to what has been observed to occur in water-saturated snow slush (Eicken, 1998). Recent

work (Maus & De la Rosa, 2012; Naumann et al., 2012) has indicated that consolidation of frazil slush can be understood in terms of removal of salt through convective overturning and progressive freezing of remaining voids. Further work to explore these processes is needed, as frazil ice growth is a key process in the interaction of ocean and atmosphere, which is of increasing importance in an ice-diminished Arctic (see Chapter 6).

1.2.5   Formation of sea ice

In the Antarctic, higher wind speeds, the effects of ocean swell penetrating from higher latitudes and the larger number of openings in the pack greatly favour the formation of frazil ice. As a result, fazil ice can constitute as much as 60–80% of the total ice thickness in some regions (Lange et al., 1989; Jeffries et al., 1994). The ice edge advances northwards from the Antarctic continent by as much as 2500 km from austral autumn through to spring (Chapter 10). This dynamic ice-growth environment favours growth of frazil ice and leads to the predominance of the so-called pancake ice (Figure 1.1). Pancake ice forms through accretion of frazil crystals into centimetre-sized floes of ice that in turn accrete into decimetre-sized pans of ice. Under the action of wind and ocean swell penetrating deep into the sea ice zone, these pans bump and grind against one another, resulting in a semi-consolidated ice cover composed of ice discs with raised edges that are from a few centimetres to more than 10 cm thick. These pancakes eventually congeal into larger units (Wadhams et al., 1987). Once the ice cover has consolidated into a continuous, solid sheet or larger floes with snow accumulated on top, only characteristic surface roughness features ('stony fields' or 'rubble ice') betray its dynamic origins. However, stratigraphic analysis of ice cores clearly demonstrates that the ice cover is largely composed of individual pancakes, often tilted or stacked in multiplets on top of one another. The interstices between the individual pancakes eventually consolidate through a combination of frazil growth and freezing of congelation ice (Lange et al., 1989). Typically, these processes account for ice thicknesses of up to 0.5 m (Wadhams et al., 1987; Worby et al., 1998).

In the Arctic, recent reductions in perennial ice extent (Chapter 11) may now increasingly favour the formation of frazil ice. The limited data available to date

do suggest an increase in the proportion of granular ice compared with previous studies (Perovich et al., 2008), but more observations are needed to confirm these early indications. In the past, most of the ice cover was composed of congelation ice (Weeks, 2010).

1.2.6 Phase relations in sea ice

Unlike zinc and copper in brass alloys, sea salts and ice do not form a solid solution in which the constituents intermingle in different proportions. Hence, the question arises as to what exactly the fate is of ions in freezing seawater. In order to fully address this problem, one needs to consider the physicochemical phase relations of an idealized or somewhat simplified seawater system.

Sodium and chloride ions (Na^+, Cl^-) account for roughly 85%, sulphate ions (SO_4^{2-}) for 8%, and magnesium, calcium and potassium for another 6% of the mass of salts dissolved in seawater. Owing to the predominance of sodium and chloride ions in seawater, many aspects of sea ice properties and structure can already be observed in a simple sodium chloride solution. More sophisticated representations of seawater typically take into account Na^+, K^+, Ca^{2+}, Mg^{2+}, Cl^-, SO_4^{2-} and CO_3^{2-}. In his classical study of the phase relations in sea ice, Assur (1960) assumed a constant 'standard' composition for sea ice. While such an approach is inadequate for geochemical studies (Marion & Grant, 1997; Chapter 17) and does present problems with ice that is strongly desalinated or grown in isolated basins, it is sufficient to predict the most important characteristics of sea ice behaviour upon cooling or warming.

Figure 1.7, taken from Assur's work, serves to illustrate the key aspects of the phase relations in sea ice. In a closed system (i.e. the mass fraction of all components is constant) one would observe that for seawater of salinity 34, cooled below the freezing point at $-1.86°C$, the ice fraction steadily increases as the temperature is lowered, assuming that the individual phases are in thermodynamic equilibrium. As the ions dissolved in seawater are not incorporated into the ice crystal lattice, their concentration in the remaining brine increases steadily. At the same time, the freezing point of the brine decreases, co-evolving with the increasing salinity of the liquid phase. At a temperature of $-5°C$, the ice mass fraction in the system amounts to 65% and the salinity of the brine in equilibrium with the ice has risen to 87. At $-8.2°C$, the concentration of salts has increased

to the point where the solution is supersaturated with respect to sodium sulphate, a major component of seawater, resulting in the onset of mirabilite precipitation ($Na_2SO_4 \cdot 10H_2O$; Figure 1.7). If one were to continue lowering the temperature of the system, mirabilite would continue to precipitate in the amounts specified in Figure 1.7. Other salts precipitating during the freezing of seawater include ikaite ($CaCO_3 \cdot 6H_2O$), the distribution and mineralogy of which we have only learned more about in very recent times (Dieckmann et al., 2010; Papadimitriou et al. 2013, 2014; Hu et al., 2014), as well as hydrohalite ($NaCl \cdot 2H_2O$). The latter is predicted to start precipitating at $-22.9°C$, with roughly 90% of the precipitable sodium chloride present as hydrohalite at $-30°C$ (Figure 1.7). While the mass fraction of brine drops below 8% at $-30°C$, even at the lowest temperatures typically encountered in sea ice (around $-40°C$), a small but non-negligible liquid fraction remains. The presence of unfrozen water even at these low temperatures has important consequences, in particular for the survival of microorganisms overwintering in sea ice (Chapters 13–16).

Salinity measurements have undergone changes throughout history (Millero et al., 2008). Originally, the saltiness of ocean water was defined as the ratio of the mass of dissolved material to the mass of the solution. However, the mass of dissolved material is difficult to measure by evaporation as many crystalline salts are bound with water and volatile components may evaporate during heating. A simplified approach has been followed since the beginning of last century, exploiting the fact that ocean water around the world is of almost uniform composition. For most of the last century, the concentration of Cl^- ions has been measured by titration and scaled linearly to salinity (sometimes quoted as ppt or ‰). This relationship is sensitive to the composition of the seawater used for calibration and was corrected slightly in the 1960s. With the advent of conductivity meters, an accurate and even more convenient way opened up for salinity measurements.

Today, the ocean salinity is measured as the ratio of the electrical conductivity of a solution to the conductivity of a reference solution and converted to a practical salinity using an equation provided by UNESCO (1978). As such, it is independent of chlorinity and mass of dissolved material. Practical salinity is defined as a dimensionless quantity and should not be quoted as

having a practical salinity unit (psu). However, this is a widespread habit in the literature. IOC et al. (2010) recommend that salinity be stored in archives according to how it has been measured, i.e. in most cases today as practical salinity.

A reference-composition salinity (reference salinity for short) has been introduced that is to be used in the most recent thermodynamic equation of state of seawater and derived properties (IOC et al., 2010). The reference salinity, S_R, is linearly related to the practical salinity u_{PS} through $S_R \approx (35.16504/35)u_{PS}$, is supposed to indicate the actual solute mass dissolved in standard seawater and is quoted in units of g kg^{-1}. IOC et al. (2010) explain that the difference between the numerical values of reference and practical salinities can be traced back to the original practice of determining salinity by evaporation of water from seawater and weighing the remaining solid material. This process also evaporated some volatile components, and most of the 0.16504 g kg^{-1} salinity difference is due to this effect.

The UNESCO salinity definitions apply to the composition of standard seawater and cover the range from 2 to 42 above –2°C. Measurements outside this range may require different equations or procedures (see IOC et al., 2010 for examples). Equations of IOC et al. (2010) are not used in this chapter.

1.3 Desalination and pore microstructure

1.3.1 Salinity profiles of growing and melting sea ice

In a pioneering study, Malmgren (1927)[1] studied the salinity evolution of Arctic first-year sea ice during the course of winter and into the summer melt season. He summarized his observations in a seminal figure that is still commonly shown 90 years after its initial publication (Figure 1.9). In this section, we will briefly consider the processes responsible for the characteristic C-shape of the salinity profile of young and first-year ice as well as the reduction in surface salinities during the first melt season in an ice floe's evolution. The importance of understanding the evolution of an ice cover's salinity profile is rooted in the central role played by temperature and salinity with respect to ice porosity and pore microstructure. Large-scale sea ice and climate
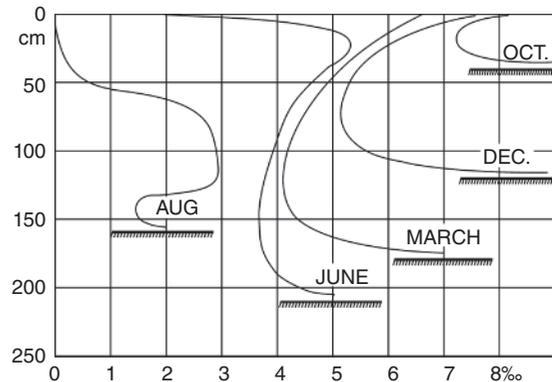
Figure 1.9 Evolution of sea ice salinity profiles (from Malmgren, 1927). Note the characteristic C-shape of the young and first-year ice salinity profile and the reduction in surface salinity due to meltwater flushing with the onset of summer melt.

models are only now beginning to move beyond the assumption of constant ice salinity (originally motivated by the prominence of multi-year sea ice in the Arctic Ocean), creating the need to better understand and simulate salinity and property evolution at the small scale in support of large-scale model efforts. For example, work by Vancoppenolle et al. (2009) found that a change of bulk salinity from 0 to 5 is equivalent to a change in sea ice albedo by 10%.

The importance of the desalination processes is illustrated by comparing the first-year winter sea ice salinity profile in Figure 1.9 with that of summer or multi-year sea ice. As dictated by the phase relationships (Figure 1.7), the transition from winter to summer sea ice generally corresponds to a change in the direction of the conductive heat flux through an ice floe from being directed upwards to being directed downwards (cf. Figure 1.10).

1.3.2 Origin of brine movement in growing sea ice

The microscopic exclusion of ions from a growing ice crystal leads to a local increase in brine salinity but does not change the local bulk salinity. However, observations clearly show that the bulk salinity of growing first-year sea ice (typically 4–6) is only a fraction of the bulk salinity of the ocean water (around 33) (Figure 1.9). Several processes have been considered to explain the reduction of the bulk salinity, i.e. the removal of ions from sea ice. The migration rate of individual brine pockets
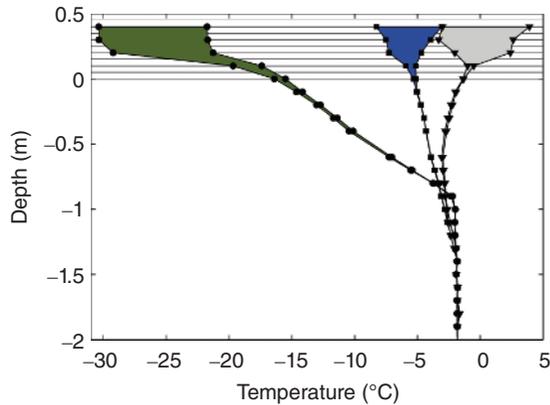
Figure 1.10 Vertical temperature profiles measured with a thermistor probe frozen into the ice in Barrow, 2008. Positive depths are snow and air, while negative depths are sea ice and ocean. Profiles show the temperature range encountered over a 24-hour period in mid-February (day 45, circles), mid-May (day 135, squares) and at the end of May (day 150, triangles).

in a temperature gradient due to solute diffusion inside the pockets was found to be too small (cf. Weeks, 2010). The significance of this process is limited to the microscopic level where it could affect the interconnectivity of the pore space. However, the impacts on that scale are still not well understood. Brine expulsion is the movement of brine in response to volume expansion during ice formation. Notz and Worster (2009) show analytically that the flow rate of brine due to volume expansion is always less than the vertical growth rate of sea ice. Hence, brine expulsion contributes only to solute redistribution in the ice but not to net desalination. This assessment applies during quasi-steady state ice growth, i.e. while the growth rate is essentially constant. A segregation process at the ice–ocean interface (often termed 'initial segregation') that had been assumed in earlier studies to parameterize sea ice salinity development (e.g. Cox & Weeks, 1988) has been found to lack empirical and theoretical basis (Notz & Worster, 2009). Hence, the only significant process contributing to the net desalination prior to the onset of melt is gravity drainage (Notz & Worster, 2009).

Hunke et al. (2011) reviewed key observations and the state of sea ice salinity modelling and found that, in spite of significant recent advances in our understanding of the processes, a simple description remained elusive. Further progress has been made since then.

Considering steady growth conditions, Petrich et al. (2011) and Rees Jones and Worster (2013) used a simple dynamical model to describe the desalination process. Reassuringly, both groups obtained the same expression for the brine flux at the ice–ocean interface. Petrich et al. (2011) were also able to derive an analytical expression for steady-state bulk salinity as a function of ice growth rate that compared well with two-dimensional (2D) computational fluid dynamics (CFD) simulations. However, based on a numerical, 1D desalination model, Griewank and Notz (2013) suggested that quantitative results of these simple quasi-steady models fall short in cases where growth conditions vary rapidly with time (e.g. insolation or diurnal temperature variations seen in spring). One could argue that the first-order description of the bulk salinity profile has been identified for quasi-steady sea ice growth (the zeroth order being depth-independent bulk salinity) and that future attention should be paid to the wide range of higher-order aspects that are relevant to sea ice microbiology, surface chemistry, radar backscatter and pollutant transport (e.g. non-quasi-steady state growth, the role of freeboard, movement of brine towards the surface, banding of inclusions). In this context it should be remembered that, in addition to processes within the ice, processes at the upper surface (e.g. meltwater pooling and vertical flushing through the ice) and beneath the ice (e.g. under-ice shear flow; Feltham et al., 2002) affect bulk salinity profile and evolution.

Let us step back and take a look at the process of natural convection. Why does brine move through sea ice to begin with? For the sake of simplicity, we treat sea ice according to the effective medium approach; we assume that the brine layers and pores in sea ice are interconnected and that no dominant channels exist; fish-tank bubbler stones have such a microstructure. Recall that brine density is primarily a function of brine salinity in sea ice (the higher the salinity, the denser the brine) and that the freezing point of brine depends on salinity (the higher the salinity, the lower the freezing point). In growing sea ice we find a temperature profile with the warmest ice near the ocean and the coldest ice at the upper surface (Figure 1.10). Thus brine salinity and brine density will increase toward the upper surface if brine and ice are in thermodynamic equilibrium. This configuration is hydrostatically unstable, i.e. a small perturbation in the density field will tend to drive flow

in a direction that further increases the magnitude of the perturbation (driving natural convection). The flow rate is retarded by friction due to the dynamic fluid viscosity, μ, of the brine and the permeability, Π, of the ice, the latter of which is a single-parameter description of the pore microstructure. While this can slow down the motion, it can, theoretically, not stop the motion. However, as a result of the dependence of the freezing point on salinity, perturbations are not in thermodynamic equilibrium with the surrounding ice. Hence, phase change will take place until thermodynamic equilibrium is obtained again and this process happens to change the brine salinity to reduce the magnitude of the density perturbation. Now, if brine movement is slow (e.g. because friction is high), perturbations can be annihilated completely due to the phase change. The rate at which phase change can take place (and perturbations are reduced) depends on the rate at which heat can be provided to or removed from the microscopic ice–brine interface. This rate is related to the thermal diffusivity of the ice α_{si} and a characteristic distance Δh for heat transport. For the sake of convenience in analytical calculations of fluid movement, a porous medium Rayleigh number can be defined for a homogeneous porous medium (Worster & Wettlaufer, 1997),

$$\mathrm{Ra} = \frac{g\Delta\rho\,\Pi\,\Delta h}{\mu\alpha_{si}} \qquad (1.1)$$

where $\Delta\rho$ is the density difference, Δh is a characteristic length and g is the acceleration due to gravity. The more the driving forces for fluid movement exceed the retarding forces, the higher the value of Ra. In fact, for natural convection to take place in a porous medium at all, the Rayleigh number has to exceed a critical Rayleigh number Ra_c (for values, see Nield & Bejan, 1998). Wettlaufer et al. (1997) demonstrated in idealized laboratory experiments that brine release from growing saltwater ice set in only after the thickness of the ice (this would be Δh in Eqn (1.1)) exceeded a threshold. It is unclear whether this effect would be observable in thin sea ice growing in its natural environment, given the ubiquity of perturbations in the ice microstructure and at its interfaces. However, heuristically extending equation (1.1) to inhomogenous sea ice (Notz & Worster, 2009) and invoking the concept of a critical Rayleigh number have led to success in 1D numerical modelling of desalination (e.g. Griewank & Notz, 2013).

1.3.3 Brine movement and bulk salinity

Mass conservation dictates that the volume of brine leaving the sea ice due to advection is balanced by brine entering the sea ice from the ocean (we neglect effects due to the density difference between ice and water here). This leads to a turbulent sea ice—ocean interface flux, i.e. an advective flux with no net direction, and there has been one attempt at determining its magnitude experimentally (Wakatsuchi & Ono, 1983). While the experiments showed that the ice–ocean interface flux increased with growth rate, the magnitude of the estimate depended on an assumed mixing factor for the experiment that the authors set by educated guesswork (they chose 0.5). Apart from its relation to the brine flux, the volume flux from the ocean into the ice determines the flux of nutrients, which is of particular relevance for biological processes (Hunke et al., 2011; Chapter 17).

Within sea ice, a downward flow increases the salinity locally, leads to local dissolution of the ice matrix and thereby creates brine channels. Locally, brine is replaced by more saline brine from above, and as the more saline brine is super-heated (i.e. above the freezing point) with respect to the temperature of the surrounding ice, it will dissolve the surrounding ice partially to attain thermodynamic equilibrium. Brine leaving through channels is detectable as distinct brine plumes (streamers) in the underlying water (Wakatsuchi, 1983; Dirakev et al., 2004). Since brine channels develop as a consequence of convection inside the porous medium, brine moving upward through the porous medium is part of the development process of channels (Worster & Wettlaufer, 1997). An upward-directed flow of brine leads to a local reduction of brine salinity, bulk salinity and porosity. Niedrauer & Martin (1979) found in laboratory experiments that downward flow follows a cusp-shape pattern that terminates in brine channels. Consistent with this general pattern of salinity distribution, Cottier et al. (1999) found in high-resolution salinity measurements that the bulk salinity is highest in the presence of brine channels and somewhat lower in between. The salinity difference between the brine leaving the sea ice and the brine entering the sea ice is the cause for the net desalination of sea ice that gives rise to the characteristic bulk salinity profiles (Figure 1.9). Hence, locally varying sea ice bulk salinity is a systematic feature of the growth process. It manifests itself as scattered data when several bulk salinity measurements are performed close to each

other on otherwise homogeneous sea ice. Gough et al. (2012) concluded that bulk salinity measurements have to differ by more than 29% to be regarded as different with 90% confidence. This means bulk salinity scatter is to be expected in a range of ±0.5 to ±1.

In growing ice, the rate of bulk desalination becomes insignificant with increasing distance from the sea ice–ocean interface. This gives rise to a quasi-steady state salinity, also termed stable salinity (Nakawo & Sinha, 1981). Two processes have been put forward to explain when bulk flow and desalination cease during ice growth. On the one hand, based on continuum fluid dynamics considerations, the permeability of sea ice may reach values too low to sustain natural convection, similar to arguments leading to equation (1.1). One the other hand, based on percolation considerations, sea ice pores may shrink and finally disconnect from regular fluid motion, retaining their solute content (or precipitates) until the melt season (see later). There are too few experimental or theoretical investigations to make a final call on the dominant process. Numerical 2D CFD simulations have reproduced observed salinity profiles either with or without assuming that the pore space disconnects (Petrich et al., 2007, 2011). The notion of a potentially disconnecting pore space in sea ice has been popularized by Golden et al. (1998). This concept enjoys popularity in the sea ice community because it gives an intuitive explanation for the observation that the sea ice bulk salinity does not change with time where porosities are below 0.05–0.07 (Cox & Weeks, 1988; Arrigo et al., 1993). The sea ice geometry is also consistent with those percolation thresholds (Petrich et al., 2006). However, as the 1D and 2D fluid dynamics simulations mentioned earlier show, the 0.05–0.07 threshold may simply result from a combination of a porosity-dependent permeability in conjunction with basic fluid and thermodynamics.

In general, fluid motion and desalination are confined to a few centimetres at the bottom of growing sea ice (Figure 1.4), possibly <5 cm in winter, but reaching 10–20 cm in spring (Petrich et al., 2013). Textbook bulk salinity profiles such as the ones in Figure 1.9 show systematic characteristics (Eicken, 1992b), such as the typical C-shape during growth, and seem to be predictable from the environmental conditions during growth (see later; Cox & Weeks, 1988). However, there is a considerable amount of variability between cores taken in close proximity (Weeks & Lee, 1962).

This variability has been attributed to pores and channels that are large compared with the sample size (Bennington, 1967; Cottier et al., 1999).

1.3.4 Development of the pore microstructure during growth and melt
In spite of its importance for optical properties, there is still no quantitative and complete description of the evolution of the pore microstructure during freezing and melt. However, we can link observations and hypotheses to understand the general process in a piecemeal approach. Here, we focus on sea ice with a columnar rather than granular texture.

The ice microstructure is lamellar close to the ocean and individual ice lamellae are interspersed with liquid brine layers or films. The separation of the lamellae is typically around 0.3–0.5 mm. As the sea ice cools or desalinates, lamellae grow thicker at the expense of brine layers and interconnect by forming bridges, presumably at porosities between 0.1 and 0.3 (see also discussion of Figure 1.11). Horizontal sections of this ice reveal inclusions ranging over several orders of magnitude in size (Perovich & Gow, 1996). What appears as large, high-aspect ratio inclusions in these images is the brine film narrowed by the ice bridges between lamellae. The bridges themselves are interspersed with smaller inclusions at all scales. All inclusions get smaller upon further cooling or desalination and the narrowed brine layers separate into even narrower films and terminate vertically. Some residual connectivity is likely throughout this pore space, at least while volume expansion during freezing creates enough pressure to push brine through the matrix. In addition to the pores between the lamellae, brine channels form that mark the preferred pathways of downward-moving brine during desalination. They are usually vertical (Figure 1.12). Their diameter can exceed the lamellae spacing and evidence is inconclusive as to what extent the lamellar structure affects the development of brine channels. Brine channels are supplied with brine through the pore network that formed between the lamellae (Lake & Lewis, 1970; Niedrauer & Martin, 1979). The direction of flow in brine channels can reverse and oscillation between inflowing and outflowing brine has been observed (Lake & Lewis, 1970; Eide & Martin, 1975). Because brine flowing upward into channels is less saline, it supports the disintegration into pores and closure at the open end, called necking (Eide

| (a) $T = -15°C$, $\phi = 0.033$ | (b) $T = -6°C$, $\phi = 0.075$ | (c) $T = -3°C$, $\phi = 0.143$ |
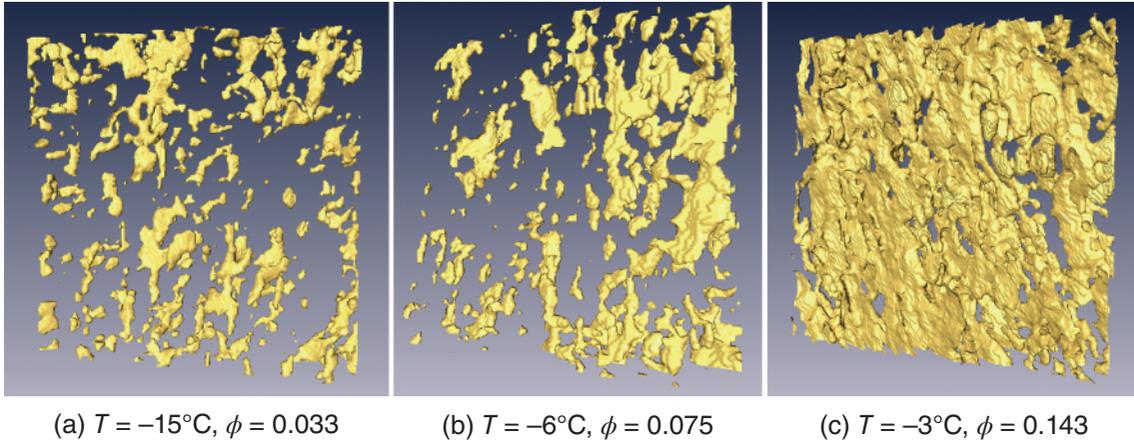
Figure 1.11 X-ray microtomography images of brine layers in sea ice single crystals as a function of temperature. Note how the sample porosity (ϕ) and connectivity increase as it is warmed. Source: Golden et al. 2007. Reproduced with permission of John Wiley & Sons.
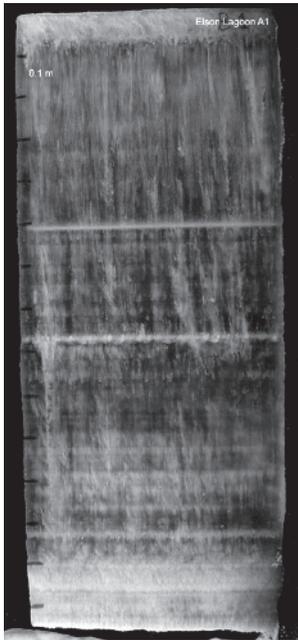
Figure 1.12 Photograph of a slab of sea ice obtained from sea ice of approximately 1.4 m thickness near Barrow, Alaska (photo courtesy of D. M. Cole). Note the distinct horizontal layering as well as the parallel rows of vertical brine channels (shown in horizontal cross-section in Figure 1.2e).

& Martin, 1975). Inclusions resembling disintegrated feeder channels are sometimes found leading towards brine channels (Lake & Lewis, 1970). They tend to be

inclined around 45° and appear mostly in the upper part of sea ice. Star-like patterns can be observed where they are visible at the ice surface (Figure 1.2e). Overall, small brine inclusions in cold sea ice show a characteristic distribution of length-to-width ratios (Light et al., 2003).

Brine inclusions enlarge upon warming during the melt season and form pathways for brine and meltwater. The slow redistribution of solute in conjunction with a drive towards thermodynamic equilibrium leads to the widening of brine channels that form preferred pathways thereafter (Polashenski et al., 2012). The pore structure of this secondary pore space differs and often contains longer and wider channels than the primary pore space of growing sea ice.

1.3.5   Brine movement during melt

The most prominent, albeit not the only, form of brine movement during the melt season is flushing of surface meltwater (Untersteiner, 1968). As the density of ice is lower than that of water, the surface of free-floating snow-free sea ice of thickness H protrudes above the water level by a distance h_f called freeboard,

$$h_f = H \left(\frac{\rho_{sw} - \rho_{si}}{\rho_{sw}} \right) \tag{1.2}$$

If sea ice is sufficiently permeable or cracks or other flaws exist, then the hydrostatic pressure of brine and meltwater (melting snow and surface ice melt) above the ocean level can result in significant transport

through the ice both vertically and laterally. Studies involving different tracers have demonstrated that the vertical and lateral transport of meltwater varies with season as a function of ice permeability. As much as a quarter of the meltwater produced annually at the surface of Arctic sea ice can be retained in pores within the ice cover (Eicken et al., 2002). The bulk salinity reduction of sea ice during melt is due to at least two processes. Infiltration of surface meltwater into the upper 0.1–0.3 m ('flushing') leads to a characteristic linear bulk salinity profile that develops in the very early stages of melt (Figure 1.13), with the lowest salinity at the top (Polashenski et al., 2012). There is modelling evidence that desalination of the lower parts of sea ice is triggered by an increase in sea ice permeability due to warming, resulting in convective overturning (Eicken et al., 2002; Griewank & Notz, 2013). The latter process is not dependent on meltwater from the surface. Repeat desalination in summer leads to extremely low bulk salinities of Arctic multi-year sea ice.

1.3.6 Permeability of sea ice

Fluid moving though sea ice experiences a resistance that is due to both microscopic obstacles in the flow path
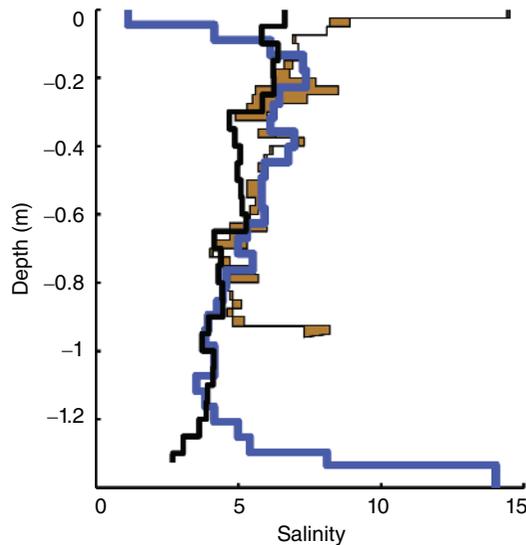
Figure 1.13 Bulk salinity profiles measured in Barrow, Alaska, at the end of May (thick line) and two profiles measured within 2 m in early February (thin lines, difference between profiles is shaded). The solid black line is the expectation based on equation (5) with growth rate from Figure 1.22.

(which lead to its tortuosity) and viscous drag along the pore and channel walls. The reciprocal of resistivity is the permeability Π, measured in m^2. Its magnitude is similar to that of the cross-sectional area of an individual duct in a 'porous' medium made up of a close-packed bundle of ducts (i.e. a porous medium consisting entirely of pathways 10^{-4} m in size would have a permeability of around $\Pi = 10^{-8} m^2$, not accounting for geometric correction factors). The volume flux q through a homogeneous porous medium can be described by Darcy's law:

$$q = -\frac{\Pi}{\mu}\frac{\partial p}{\partial x} \tag{1.3}$$

where μ is the dynamic viscosity and $\partial p/\partial x$ is the pressure gradient in the direction of flow. The permeability tensor is generally anisotropic in sea ice, i.e. its components depend on the direction of flow; this is due to the anisotropic crystal fabric and pore structure which provide the highest permeability in the vertical direction. Differences of about one order of magnitude seem to be typical (Freitag & Eicken, 2003). While the permeability of the open ocean is infinite, we can expect that the vertical permeability at the bottom of the skeletal sea ice layer remains finite even as the porosity approaches 1: the regularly spaced ice lamellae, no matter how thin, will exert drag forces on the brine moving past.

In fact, the pore space may get clogged to some extent and flow patterns are altered by gelatinous extracellular polymeric substances (EPS) secreted by ice-dwelling organisms (Chapters 13 and 17; Krembs et al., 2011). The influence of EPS on the development of sea ice microstructure and bulk salinity has received little attention from researchers so far.

A possible permeability–porosity relationship for growing sea ice that is consistent with field measurements (Freitag, 1999; Eicken et al., 2004) and effective medium theory (Golden et al., 2007) is

$$\Pi = \Pi_0 \left(\frac{V_b}{V}\right)^3 \tag{1.4}$$

where Π_0 is of the order of $\Pi_0 = 1...3 \times 10^{-8} m^2$ and V_b/V is the brine volume (porosity) of the ice. The value of Π_0 depends on whether we consider one component of the permeability tensor in unidirectional flow or an equivalent isotropic permeability for multidimensional flow. The equivalent isotropic permeability is usually taken to be the geometric mean of the individual component. Due to the development of a secondary

pore space during melt (e.g. large brine channels), the permeability–porosity relationship will probably depend on the history of the ice. In fact, fluid flow through very wide brine channels cannot be described as porous medium flow, as momentum conservation of draining water starts to become apparent (cf. Polashenski et al., 2012).

1.3.7   Sea ice salinity parameterizations

Sea ice bulk salinity is a core state variable of sea ice, and most models of sea ice properties depend on it in some form. As it depends on many aspects of the growth environment, early parameterizations were empirical, statistical correlations based on field measurements or laboratory experiments. One of the first complete, numerical models of sea ice bulk salinity development was motivated by ice strength calculations (Cox & Weeks, 1988). One decade later, salinity modelling started to see a renaissance, probably motivated in part by the advent of general circulation models, climate change and associated scientific interest in sea ice.

Bulk salinity parameterizations take advantage of a steady-state bulk salinity ('stable salinity') that is attained after a few days in growing ice. Most parameterizations are either statistical correlations (Kovacs, 1996; Petrich et al., 2006) or are based on curve-fitted equations derived from theoretical considerations (Nakawo & Sinha, 1981 – following an expression after Burton et al., 1953). Both the equation after Burton et al. (1953) and statistical parameterization typically relate steady-state bulk salinity to growth rate.

Recently, a new type of parameterization was suggested that is based on the analytical solution of the mass conservation equation of gravity-driven fluid motion in sea ice (Petrich et al., 2011). To facilitate this, constant growth rate and a highly simplified permeability profile of sea ice were assumed (i.e. finite and zero permeability above and below a specified porosity threshold, respectively). The results compared favourably with 2D CFD simulations and are reported here for their novel character. The steady-state bulk salinity of sea ice, S_{ice}, growing from seawater of salinity, S_0, is:

$$\frac{S_{ice}}{S_0} = \frac{\rho_0}{\rho_i}\phi_c\left(1 + \frac{h}{z_x}\right) \tag{1.5}$$

where ρ_0 and ρ_i are density of seawater and freshwater ice, respectively, ϕ_c is a critical porosity below which

sea ice does not desalinate, and h/z_x is the dimensionless thickness of the desalinating layer,

$$\frac{h}{z_x} = \frac{\phi_c}{2}\frac{v}{\gamma_s w_0}\left[-1 + \sqrt{1 + \frac{2(1 - \phi_c)}{\phi_c^2}\frac{\gamma_s w_0}{v}}\right] \tag{1.6}$$

where v is the vertical growth rate of the ice, w_0 is a velocity scale defined as

$$w_0 = \frac{\Pi}{\mu}g\frac{\partial\rho}{\partial C}C_0 \tag{1.7}$$

where C_0 is the solute concentration of seawater, g is the acceleration due to gravity, Π the permeability in the layer of porosity larger than ϕ_c, and γ_s an undetermined parameter that has to be fitted. They set $\phi_c = 0.05$ and determined $\gamma_s w_0 = 4.5 \times 10^{-8}$ m s^{-1} from comparison with 2D CFD model simulations ($C_0 = 34$ kg m^{-3}). Figure 1.13 shows correspondence of growth rate and steady-state bulk salinity from equation (1.5) with data obtained at Barrow, Alaska, in 2008. A feature common to statistical correlations, the relationship after Burton et al. (1953) and equation (1.5) is that the salinity–growth rate dependence approximates a power law, where bulk salinity increases with growth rate. While parameterizations can give a first estimate of bulk salinity, they do not allow for the wide range of variable growth conditions that 1D or 2D numerical simulations can cover explicitly.

1.3.8   Phase fractions and microstructural evolution

A phase diagram, such as that shown in Figure 1.7, in itself contains no direct information on the (microscopic) configuration of individual phases within the system, i.e. its microstructure. In the case of growing, natural sea ice, the latter depends on two principal factors, the growth environment and the boundary conditions at the advancing ice–water interface at the time of growth (Figure 1.4), and the *in situ* temperature and chemical composition of the ice horizon under consideration. This second controlling factor leads to a temperature-dependent porosity and is of prime importance for a wide range of ice properties considered in Section 1.4. Owing to the stark contrast in physical properties between ice, brine, salts and gas inclusions, knowledge of their relative volume fraction can provide us with an estimate of the bulk (macroscopic) properties of sea ice. For example, the mechanical strength of

sea ice depends strongly on the relative brine and gas volume fraction, because these two phases effectively have no strength.

A specific example of the microstructural evolution of sea ice as a function of temperature is given in Figure 1.8, which shows the relative volume fraction and microstructure of elongated pores in a core sample of columnar sea ice. The data for these images were obtained using magnetic resonance imaging (MRI) of samples at the indicated temperature. This permitted the microstructural evolution of brine-filled pores to be followed without disturbing or destroying the sample. One particular challenge common to most studies of ice microstructure and properties is the strong dependence of the relative liquid pore volume on temperature. Commonly, samples are cooled to temperatures below –20°C immediately after sampling to avoid loss of brine from the sample, which would also strongly affect properties and microstructure. As evident in Figures 1.8 and 1.11, such temperature changes strongly affect the pore microstructure. Hence it requires either special sampling and sample preparation techniques or non-destructive methods, such as MRI or X-ray tomography, to actually obtain insights into the pore microstructure at the *in situ* temperature (Eicken et al., 2000; Pringle et al., 2009).

As the sample is warmed from its *in situ* temperature, at which it was maintained for the entire period after sampling, the brine volume fraction increases as prescribed by the phase relations. At the same time, however, the size, morphology and connectivity of pores evolve, with pores visibly linking up at higher temperatures (–6°C; Figure 1.8). This process of inter-connecting pores of reasonable size as the temperature increases above a critical threshold (for a given salinity) is an important aspect of microstructural evolution and of great importance for sea ice transport properties, such as permeability. In a recent study that combines different modelling approaches and high-resolution X-ray microtomography, Golden et al. (2007) have further examined these linkages between pore connectivity and permeability. The X-ray microtomography data clearly show how sheets of brine segregate into disjunct, isolated pores at low temperatures and how they start to link up at higher temperatures (Figure 1.11). It is important to note that these microtomography images and more detailed data on pore morphology and connectivity derived from them (Pringle et al., 2009),

illustrate that the classic pore-space model developed by Assur (see the discussion in Section 1.4) is not sufficient for modelling of ice transport properties.

1.3.9   Temperature and salinity as state variables

From the phase relations (as summarized in Figure 1.7), it follows that the relative volume fraction of brine depends solely on the ice temperature, T, and its bulk salinity, S_{si}, provided the volume is isothermal and in thermodynamic equilibrium and given the pressure (usually atmospheric) and composition of the brine (usually 'standard' composition). The salinity of the brine, S_b, contained within such an ice volume would similarly be prescribed by the phase relations. Hence, temperature and salinity of the ice are the prime controlling or state variables governing not only the phase fractions but, as outlined below, a whole host of other physical properties. Here, use of the term 'state variable' occurs in a very loose sense, as formulation of a true equation of state for sea ice has been elusive to date. For deeper insight into the problem and recent progress, see IOC et al. (2010).

The thermodynamic coupling between these different variables is a key aspect of sea ice as a geophysical material and a habitat. Any temperature change directly affects the porosity and pore microstructure of the ice, as well as the salinity and chemical composition of the brine. Direct measurement of these properties in the field is difficult. Commonly, the *in situ* brine volume fraction and other properties are derived from the bulk salinity of an ice sample and its *in situ* temperature. The latter can be measured by inserting temperature probes into freshly drilled holes in a core or with sensors frozen into the ice. The bulk salinity is typically obtained by dividing an ice core into sections, melting these in the laboratory and then deriving the salinity from electrolytical conductivity measurements. Ideally, one would also measure the density of a sea ice sample, ρ_{si}, in order to determine the air volume fraction V_a/V. In fresh ice, this is typically much smaller than the brine volume fraction, but it can be substantial in multi-year or deteriorated ice, in particular above the water line (Timco & Weeks, 2010).

From the data compiled by Assur (1960) for the phase relations[2] and based on the continuity equations for a multi-phase sea ice mixture, Cox and Weeks (1983) derived a rather useful set of equations describing the

brine volume fraction as a function of ice tempera-
ture and salinity. Thus, the brine volume fraction is
derived as:

$$\frac{V_b}{V} = \left(1 - \frac{V_a}{V}\right)\frac{(\rho_i/1000)S_{si}}{F_1(T) - (\rho_i/1000)S_{si}F_2(T)} \quad (1.8)$$

The density of pure ice is given as:

$$\rho_i = 917 - 0.1403T \quad (1.9)$$

with ρ_i in kg m^{-3} and T in °C. $F_1(T)$ and $F_2(T)$ are empir-
ical polynomial functions $F_i(T) = a_i + b_i T + c_i T^2 + d_i T^3$, based on the phase relations. The coefficients for
different temperature intervals are listed in Table 1.1.
The brine salinity and density can be approximated for
temperatures above −23°C as:

$$S_b = F_3(T) \quad (1.10)$$

$F_3(T)$ is an empirical polynomial function $F_3(T) = a_3 + b_3 T + c_3 T^2 + d_3 T^3$, based on the phase relations.

The relationships in equations (1.8) and (1.10) give
rise to the 'rule of fives' (Golden et al., 1998), which
states that in first-year sea ice that formed from ocean
water (rather than less saline brackish water) with bulk
salinity around $S_{si} = 5$, the porosity is 5% when the ice
temperature is near $T = -5°C$. The phase relationship
(equation 1.8) is illustrated in Figure 1.14 in the absence
of air. Note that the porosity of cold ice is generally

small. The brine density ρ_b (in kg m^{-3}) depends on brine
salinity S_b according to:

$$\rho_b = 1000 + 0.8S_b \quad (1.11)$$

Equations (1.8)–(1.11) thus provide us with a simple
tool to derive key quantities of importance for a wide
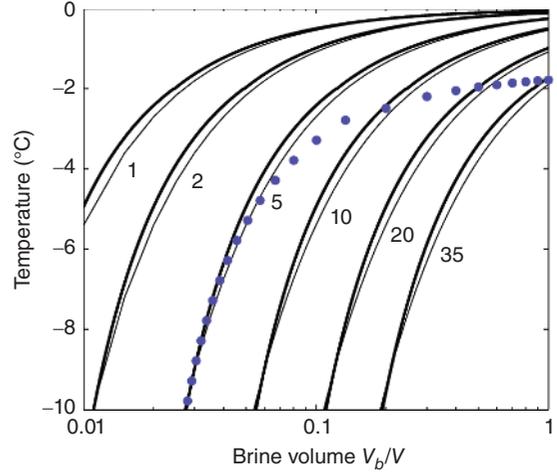
Figure 1.14 Relationship between brine volume fraction and
temperature T for various values of bulk sea ice salinity S_{si}.
The thick line is after Cox and Weeks (1983), and the thin
line follows the linearized relationship $V_b/V = m S_{si}/T$, with
$m = -0.054$ K^{-1}. The dots are an artist's impression of a possible
desalination pathway in growing sea ice.

Table 1.1 Coefficients for functions $F_1(T)$, $F_2(T)$ and $F_3(T)$ for different temperature intervals. Source: From Cox & Weeks (1983),
Leppäranta & Manninen (1988) and Cox & Weeks (1986).

T (°C)	a_1	b_1	c_1	d_1
$0 \geq T > -2$	−0.041 221	−18.407	0.584 02	0.214 54
$-2 \geq T \geq -22.9$	−4.732	−22.45	−0.6397	−0.010 74
$-22.9 > T \geq -30$	9899	1309	55.27	0.7160

T (°C)	a_2	b_2	c_2	d_2
$0 \geq T > -2$	0.090 312	−0.016 111	1.2291×10^{-4}	1.3603×10^{-4}
$-2 \geq T \geq -22.9$	0.089 03	−0.017 63	-5.330×10^{-4}	-8.801×10^{-6}
$-22.9 > T \geq -30$	8.547	1.089	0.045 18	5.819×10^{-4}

T (°C)	a_3	b_3	c_3	d_3
$0 \geq T > -2$	−0.031 6891	−18.3801	0.327 828	0.213 819
$-2 \geq T \geq -22.9$	−3.9921	−22.700	−1.0015	−0.019 956
$-22.9 > T \geq -30$	206.24	−1.8907	−0.060 868	−0.001 0247

range of physical, biological and chemical studies of sea ice.

1.3.10 Caveats and limitations

In arguing the case for the overriding importance of temperature and salinity in determining ice properties, microstructural studies and geochemical analysis indicate that chemical fractionation cannot always be ignored. Consequently, microscopically the fluid composition in sea ice may deviate significantly from its bulk composition, impacting phase evolution, pore microstructure and dependent properties. Such deviations from the evolution of a microscopically homogeneous system are potentially also of significance for biological and chemical processes within the ice cover. Improvements in analytical techniques, with development of *in situ* earth magnetic field nuclear magnetic resonance (NMR) spectroscopy as a particularly interesting example (Callaghan et al., 1999) and advances in geochemical modelling of aqueous solutions at low temperatures (Marion & Grant, 1997; Marion & Kargel, 2008), hold considerable promise in resolving some of these issues. Geochemical modelling is particularly useful, as it allows us to easily treat systems of different chemical composition, whereas the empirical approach outlined earlier is only valid for a single system of a given, standard composition.

1.4 Physical properties

1.4.1 Thermal conductivity

The thermal properties control the magnitude of heat flow through the ice cover and determine its rate of response to variations in surface or bottom forcing. The conductive heat flux through an ice cover, F_c, is given by the product of sea ice thermal conductivity, λ_{si} and the temperature gradient, dT/dz

$$F_c(z) = -\lambda_{si}\left(\frac{dT}{dz}\right)_z \qquad (1.12)$$

The thermal conductivity of pure ice as a function of temperature is given by Yen et al. (1991) as:

$$\lambda_i = 1.16 \text{ W m}^{-1}\text{K}^{-1} \times (1.91 - 8.66 \times 10^{-3}T$$
$$+ 2.97 \times 10^{-5}T^2) \qquad (1.13)$$

with T in °C. At 0°C λ_i is approximately 2.0 W m^{-1} K^{-1}. The thermal conductivity of brine, on the other hand, is

lower by a factor of roughly 4 and can be approximated by:

$$\lambda_b = 0.4184 \text{ W m}^{-1}\text{K}^{-1}(1.25 + 0.030T + 0.00014T^2) \qquad (1.14)$$

with T in °C (Yen et al., 1991). The differences in thermal conductivity of ice and brine (and air, if present) make sea ice bulk thermal conductivity sensitive to porosity. Schwerdtfeger (1963) and Ono (1968) developed a model for the thermal conductivity of sea ice based on the thermal properties of the pure end-members, ice and brine, and assumptions about the ice microstructure. For vertically oriented, parallel lamellar brine inclusions, one arrives at the following dependence of λ_{si} on brine volume (no gas inclusions) in a direction parallel to the lamellae:

$$\lambda_{si} = \lambda_i - (\lambda_i - \lambda_b)\frac{S_i\rho_{si}}{m\rho_b T} \qquad (1.15)$$

with sea ice salinity S_i, bulk sea ice and brine density, ρ_{si} and ρ_b, respectively, temperature T (in °C) and $m < 0$ the slope of the phase boundary in the phase diagram (Figure 1.7). Note that the fraction in equation (1.15) is a function of the porosity of the ice (cf. Section 1.3). Hence, in this physical configuration, the magnitude of λ_{si} does not depend on the actual size or distribution of the inclusions but only on their mass fraction. Ono (1968) and Schwerdtfeger (1963) also considered the impact of spherical gas inclusions on λ_{si}. These are typically of minor importance in first-year ice, as gas volume fractions are mostly an order of magnitude lower than those of brine.

Untersteiner (1961) introduced a simple parameterization as a function of ice temperature, T, and salinity, S_{si}, that has been employed in some ice-growth models (Maykut, 1986):

$$\lambda_{si} = \lambda_i + 0.13\frac{S_{si}}{T} \qquad (1.16)$$

Both equations (1.14) and (1.16) are functionally identical to the continuum approach in Section 1.3 which postulates for porosity V_b/V in thermodynamic equilibrium:

$$\lambda_{si} = \lambda_i + (\lambda_b - \lambda_i)\frac{V_b}{V} \qquad (1.17)$$

Recently, accurate measurements of the thermal conductivity of sea ice have been performed by Pringle et al.

(2007). They give the thermal conductivity as:

$$\lambda_{si} = \frac{\rho_{si}}{\rho_i}\left(2.11 - 0.011T + 0.09\frac{S}{T} - \frac{\rho_{si} - \rho_i}{1000}\right)\ \text{W m}^{-1}\ \text{K}^{-1}$$

(1.18)

with T in °C and ρ_{si} and ρ_i (in kg m⁻³) the densities of sea ice and pure ice, respectively.

1.4.2   Specific heat capacity and latent heat of fusion and of sea ice

The specific heat capacity describes the relationship between an amount of energy, ΔQ, added to a system of mass M and the temperature change, dT, it experiences:

$$\Delta Q = M\,c\,dT$$

(1.19)

As a temperature change of sea ice is always accompanied by a phase transition at the pore scale, the apparent heat capacity of sea ice, c_{si}, is larger than the heat capacity of pure ice, c_i. Given an expression for the apparent heat capacity of sea ice, temperature changes of sea ice can be calculated conveniently from equation (19). Malmgren (1927) introduced an expression for the sea ice heat capacity as a function of heat capacities of ice, brine and water and latent heat released due to phase transition under the assumption of thermodynamic equilibrium and constant bulk salinity. Ono (1967) simplified the expression of Malmgren by assuming a linear relationship between brine salinity and temperature for $T > -8.2$ °C (the onset of mirabilite precipitation), yet allowed for a temperature dependence of the heat capacity of ice and water. The most significant terms in his result are:

$$c_{si} = c_i + \beta T - m_m L\frac{S_{si}}{T^2}$$

(1.20)

where he used $c_i = 2.11$ kJ kg⁻¹ K⁻¹ for the specific heat capacity of ice at 0°C, $\beta = 7.5$ J kg⁻¹ K⁻² as temperature coefficient of the heat capacity of ice; $L = 333.4$ kJ kg⁻¹ for the latent heat of fusion of freshwater; and $m_m = -0.05411$ K for the slope of the liquidus curve. S_{si} is the bulk salinity of sea ice and T the temperature in °C. Previously, Untersteiner (1961) proposed an empirical relationship for the heat capacity of sea ice:

$$c_{si} = 2.11\ \text{kJ kg}^{-1}\text{K}^{-1} + 17.2\ \text{kJ K kg}^{-1}\frac{S_{si}}{T^2}$$

(1.21)

which is in line with Ono's (1967) result.

It is instructive to trace the origin of this relationship. The specific heat capacity at constant pressure can be expressed in terms of enthalpy (internal energy) H as:

$$c_{si} = \frac{1}{M}\left(\frac{dH}{dT}\right)_P$$

(1.22)

where M is the mass containing H. Including sensible heat of liquid and ice and latent heat of fusion, L:

$$H = M[c_w T f_m + c_i T(1 - f_m) - (1 - f_m)L]$$

(1.23)

where c_w and c_i are the specific heat capacity of liquid and ice, respectively (assumed to be temperature-independent) and f_m is the liquid mass fraction in thermodynamic equilibrium:

$$f_m = m_m \frac{S_{si}}{T}$$

(1.24)

We keep the bulk sea ice salinity S_{si} fixed, insert equation (1.24) into 1.23 and differentiate following equation (1.22) to obtain:

$$c_{si} = c_i - m_m L\frac{S_{si}}{T^2}$$

(1.25)

Equation (1.25) is consistent with the result of both Ono (1967) and Untersteiner (1961); it is curious to see that the heat capacity of sea ice does not explicitly depend on the heat capacity of the liquid. This is due to the assumptions of a linear phase relationship (equation 1.24) and constant bulk salinity, which render the sensible heat term of the liquid (the first term in equation 1.23) independent of temperature, i.e. the heat contained in the (variable) liquid mass does not change during temperature change. We should emphasize that the equations given for the specific heat capacity apply to the case of constant bulk salinity only, i.e. not during initial ice formation near the ice–ocean interface. For the sake of simplicity, assuming the bulk salinity decreased linearly as the ice temperature decreases from –2 to –5 °C, we estimate that the effective heat capacity during initial desalination of sea ice could be twice as high as stated in equations (1.20) and (1.21). Given that the heat capacity depends on bulk salinity and that bulk salinity changes with time, it may be easier to perform an energy balance calculation of growing ice based on the effective latent heat of fusion of sea ice, as discussed later.

As is evident from equation (1.21) and from Figure 1.15 showing measurements of c_{si} as a function
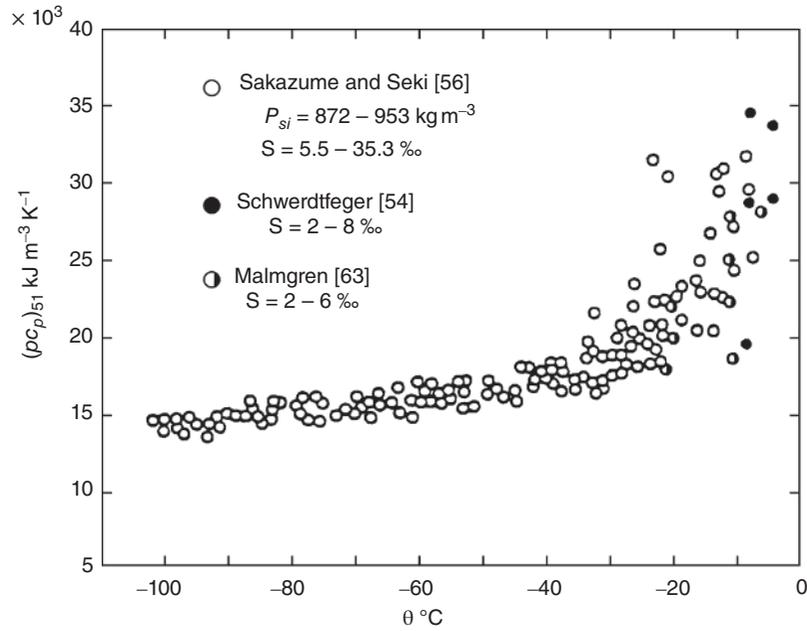
Figure 1.15 Effective specific heat capacity of sea ice c_p (shown as product of c_p with ice density ρ) as a function of temperature θ. Source: Yen et al., 1991.

of temperature, the specific heat capacity increases substantially above about −5°C. This increase implies that it takes substantially more energy to warm an ice cover by 1 K at a temperature close to the freezing point of seawater than at, say, −10°C. The effect of latent heat on temperature change has been found to be crucial for the calculation of the sea ice mass balance in large-scale sea ice or climate models (cf. Vancoppenolle et al., 2009). It also affects the pore space, permeability (and, by extension, albedo), radar signal and optical scattering properties of the ice.

The diffusive propagation of a temperature signal in sea ice can be determined from the heat transfer equation, describing the change in temperature with time dT/dt in terms of c_i, λ_i and ρ_i. In one dimension:

$$\rho_i c_{si} \frac{dT}{dt} = \frac{\partial}{\partial z}\left[\lambda_{si}\frac{\partial T}{\partial z}\right] \qquad (1.26)$$

Note that equation (1.26) is energy-conserving, but does not account for density differences between liquid and solid and associated fluid movement. For a medium of homogeneous thermal properties:

$$\frac{dT}{dt} = \frac{\lambda_{si}}{\rho_{si}c_{si}}\frac{\partial^2 T}{\partial z^2} \qquad (1.27)$$

The term $(\lambda_{si}/c_{si}\rho_i)$ is commonly referred to as the sea ice thermal diffusivity and describes the rate at which a temperature fluctuation propagates through the ice. It is over an order of magnitude larger in cold ice than it is near the freezing/melting point of sea ice.

The specific heat capacity of sea ice is a useful concept to calculate the temperature change within the ice without the need to consider porosity changes and latent heat explicitly. Similarly, a latent heat of fusion of sea ice can be derived to facilitate the calculation of growth and ablation rates without the need to consider porosity and sensible heat explicitly (Bitz & Lipscomb, 1999; Section 1.5). In this sense, the latent heat of fusion of sea ice can be defined as the temperature integral of the specific heat capacity. This is the difference between the enthalpy of sea ice at a given temperature and salinity and the enthalpy when all the ice is melted at temperature $T_F = m_m S_{si}$. Thus:

$$-L_{si}M = H(T, S_{si}) - H(T_F, S_{si}) \qquad (1.28)$$

and using equations (1.23) and (1.24) we find:

$$L_{si} = L - c_i T + c_i m_m S_{si} - m_m L \frac{S_{si}}{T} \qquad (1.29)$$

Equation (1.29) contains the dominant terms of the expression derived by Ono (1967). His result is derived from integrating the specific heat capacity of sea ice from temperature T to the melting point of sea ice, keeping bulk salinity S_{si} constant. The most significant terms are:

$$L_{si} = \left(333.4 - 2.11T - 0.114S_{si} + 18.1\frac{S_{si}}{T}\right) \text{ kJ kg}^{-1}$$

(1.30)

The latent heat of fusion of sea ice takes into account both the reduction of the latent heat due to finite porosity and the transfer of sensible heat between brine and ice. For example, the combined amount of sensible and latent heat required to completely melt sea ice amounts to 246 kJ kg^{-1} at a temperature of $T = -2°$C and a salinity of $S_{si} = 10$.

While equations (1.29) and (1.30) apply only to melting sea ice, the effective latent heat for freezing ice can be obtained similarly if we assume $T_F = m_m S_0$ of the initial liquid of salinity S_0. The result is:

$$L_{si} = L - c_i T + c_i m_m S_{si} - m_m L \frac{S_{si}}{T} + c_w m_m (S_0 - S_{si}) \quad (1.31)$$

Comparing equations (1.29) and (1.31), we find that the effective latent heat of fusion of sea ice is about 2% smaller during ice growth than it is during melt; this is because ocean water of $-2°$C is closer to the temperature of cold ice than the temperature at which all ice (now of bulk salinity below seawater salinity) will be melted. Applications for both sea ice latent heat and heat capacity are given in Section 1.5.

With a liquid phase present in sea ice down to temperatures as low as $-55°$C (Figure 1.7), sea ice is freezing and melting at a microscopic level whenever temperatures change. However, at a macroscopic level, sea ice melt is typically associated with rotting and disintegration of ice floes, largely confined to spring (Petrich et al., 2012a).

1.4.3   Optical properties of sea ice

The pore structure of sea ice has a profound influence on its optical properties, and the physics of absorption and scattering and their relationship with apparent optical properties are described in detail in Chapter 4. Briefly, light is scattered at optical inhomogeneities, in particular air and brine inclusions and precipitated salts (Chapter 4). Light scattered back to the atmosphere gives rise to sea ice albedo (Figure 1.16), while transmitted light is of paramount importance to sea ice microbiota occupying the lower centimetres of Arctic sea ice in spring, sea ice decay and the under-ice light environment. The thin section photographs in Figure 1.2 and the different ice types shown in Figure 1.1 provide some indication of the complexity of the topic of radiative transfer between atmosphere, ice and ocean. Backscatter, absorption and transmission depend on the relative contribution of microscopic absorption and scattering along the path of individual photons (Chapter 4; Perovich, 1998).

While the light field at the underside of sea ice is an important environmental factor for ice and ocean biology, the interpretation of field measurements is challenged by both the anisotropy of the scattering coefficient and the general inhomogeneity of the ice cover. The scattering coefficient of sea ice is highly anisotropic, meaning the probability of scattering is
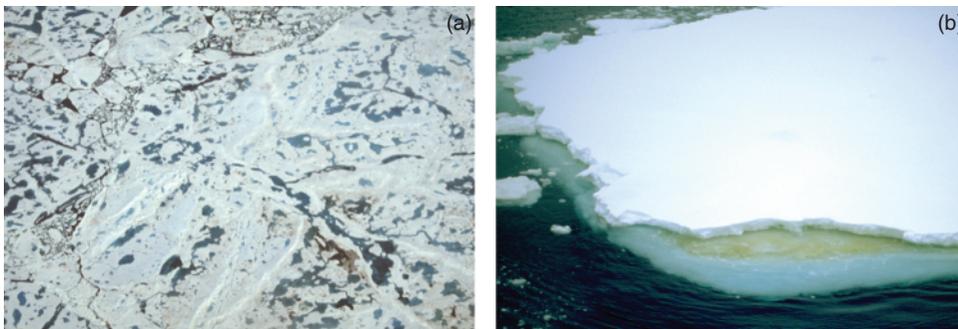
Figure 1.16   (a) Surface of summer Arctic sea ice, aerial photograph, several hundred metres wide. (b) Summer Antarctic sea ice, ship-based photograph, approximately 20 m wide. Note the high albedo of snow-free, well-drained surface ice and the low albedo of the melt ponds in (a). The brown discoloration of the ice visible at freeboard level in (b) is due to high concentrations of sea ice algae in an infiltration layer (Chapter 14).

lower for light travelling vertically through sea ice than for light travelling horizontally (Buckley & Trodahl, 1987; Katlein et al., 2014). This affects the angular distribution of light transmitted through sea ice and has ramifications for the quantitative interpretation of under-ice light measurements (Katlein et al., 2014). At the same time, sea ice and surface optical properties are inhomogeneous, most apparent in the form of snow drifts and melt ponds (Chapter 4).

However, rules on light propagation can be derived that give guidance as to where or how transmission measurements should be performed. For example, under overcast conditions and in a spectral range of low absorption (i.e. blue and green), 10% and 90% of the flux detected under ice is incident on the surface within a radius of less than 0.3 and two times the ice thickness, respectively (Petrich et al., 2012b). Hence, if surface and ice conditions of 1 m thick ice are homogeneous over a radius of 2 m, ice and surface can be treated as homogeneous for the purpose of light transmission measurements. Conversely, a strong surface perturbation of 0.3 m radius directly above the point of measurement will alter the measurements by 10% at most. Transmission measurements near the edge of melt ponds have been found to be consistent with Monte Carlo simulations (Ehn et al., 2011; Petrich et al. 2012b).

1.4.4 Dielectric properties of sea ice

The dielectric properties of sea ice govern the propagation and attenuation of electromagnetic waves which in turn determine both the optical properties of sea ice and sea ice signatures in remote-sensing data sets (Chapter 9). For a detailed treatment of electromagnetic wave propagation in lossy dielectric media, see Schanda (1986) and Hallikainen & Winebrenner (1992).

For an electromagnetic wave propagating in z-direction at the time t, the electric field, E_x, in the x-direction is given by:

$$E_x = E_0 \cos(\omega t - kz) \qquad (1.32)$$

where E_0 is the field at $z = 0$, k is the wave number and ω the angular frequency. Maxwell's equations yield the speed of wave propagation (v) in a medium with the relative electric permittivity, ε, and relative magnetic permeability, μ, as:

$$v = \frac{c}{\sqrt{\varepsilon \mu}} \qquad (1.33)$$

with the speed of light in terms of the permittivity and permeability of free space:

$$c = \frac{1}{\sqrt{\varepsilon_0 \mu_0}} \qquad (1.34)$$

The relative (dimensionless) permittivity ε, also referred to as the dielectric constant, is a complex variable for a medium in which electromagnetic waves are absorbed (a so-called lossy medium), such that

$$\varepsilon = \varepsilon' - i\varepsilon'' = \varepsilon'(1 - i \tan \delta), \qquad (1.35)$$

with i denoting the complex part of the permittivity and $i^2 = -1$; ε' describes the contrast with respect to free space ($\varepsilon'_{air} = 1$) and tan δ is the so-called loss tangent.

In a non-polar medium, ε' and ε'' are constants, whereas in substances in which the molecules exhibit a permanent dipole moment (e.g. water), ε' and ε'' are frequency-dependent because resonance affects wave decay. Ionic impurities present in seawater and brine also affect the propagation of electromagnetic waves, such that ε'' depends on the conductivity σ:

$$\varepsilon'' = \frac{\sigma}{\varepsilon_0 \omega} \qquad (1.36)$$

(Figure 1.17). Ignoring scattering and assuming a homogeneous medium, one can assess the penetration depth, δ_p, of electromagnetic radiation of a given frequency as

$$\delta_p = \frac{1}{\kappa_a} = \frac{\sqrt{\varepsilon'}}{k_0 \varepsilon''} \qquad \text{for } \varepsilon' \ll \varepsilon'' \qquad (1.37)$$

The attenuation of electromagnetic waves can be described in simplified terms by an extinction coefficient κ, with separate contributions from absorption, κ_a, and scattering, κ_s, similar to the sea ice optical properties. In particular in the single scattering approximation, $\kappa = \kappa_a + \kappa_s$. Despite its gross simplification of radiative transfer, the concept of a penetration depth can help in the interpretation of remote-sensing data, such as radar or passive microwave imagery (Chapter 9). Thus, it is of particular relevance for remote sensing of the oceans and sea ice that the dielectric loss factor ε'' of water varies by more than one order of magnitude in the 1–100 GHz frequency range. Furthermore, at frequencies < 10 GHz, ε'' differs by as much as one order of magnitude for freshwater and seawater or brine, due to the impact of ionic impurities on wave decay. Hence, penetration depths at typical radar or
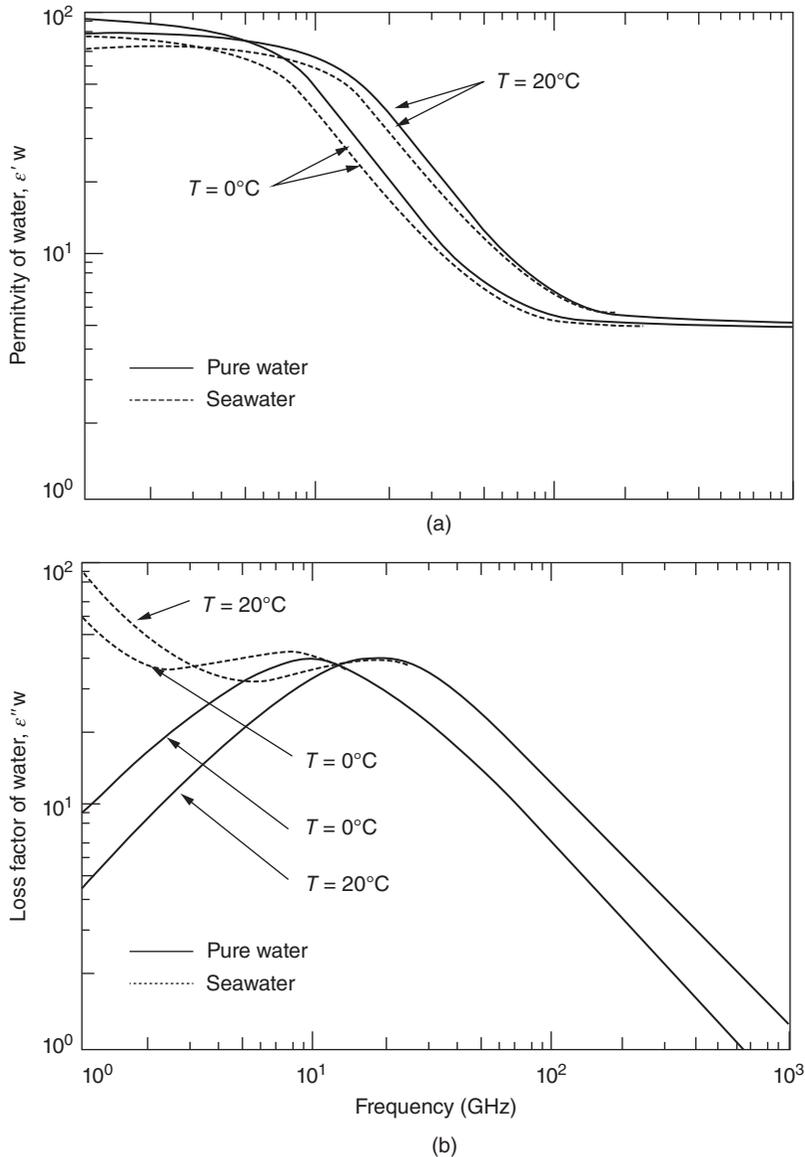
Figure 1.17 Permittivity (a) and loss factor (b) for pure water and seawater at microwave frequencies. Source: Hallikainen & Winebrenner, 1992. Reproduced with permission of John Wiley & Sons.

passive-microwave frequencies are in the order of millimetres to centimetres in seawater. For pure, cold ice ε' is constant at 3.17 for frequencies between 10 MHz and 1000 GHz, whereas ε'' is up to several orders of magnitude smaller than that of water. Consequently, one can derive the dielectric properties of sea ice from the properties of its constituent phases based on an underlying microstructural model (Stogryn, 1987), specifying the shape, size and distribution of brine inclusions as well as their volume fraction. Rather than describing ice microstructure in highly idealized terms such as the Stogryn model, Lin et al. (1988) have derived the emissivity of sea ice at microwave frequencies based on a stochastic representation of sea ice microstructure. In

this approach, the sub-parallel arrangement of brine layers within individual ice crystals (Figures 1.4 and 1.5) is rendered in terms of the autocorrelation length of the two-dimensional autocorrelation function.

In simpler, empirical approaches, ε has been parameterized as a function of the fractional brine volume (Hallikainen & Winebrenner, 1992), which in turn is determined by the temperature and salinity of the ice (Section 1.3). The extent to which temperature and ice salinity dominate the penetration depth is illustrated in Figure 1.18. At temperatures of around $-5°C$, radar waves can thus penetrate several tens of centimetres to more than a metre into low-salinity multi-year ice, whereas penetration depths in saline first-year ice are only on the order of a few centimetres at most. Under such conditions, the radar backscatter signatures of multi-year are dominated by volume scattering from gas bubbles and brine inclusions. In first-year and young sea ice, ice surface scattering predominates and radar backscatter coefficients are mostly determined by the surface roughness of the ice. This allows for discrimination of generally smooth first-year ice and multi-year sea ice in radar satellite imagery. Owing to the polarization and frequency dependence of the dielectric properties (Figure 1.18), more sophisticated multi-frequency and multi-polarization instruments can be of considerable use in distinguishing between different ice types. The same principles apply to thermal emission at microwave frequencies from different ice types and form the basis for commonly employed algorithms in discriminating between first- and multi-year sea ice in passive-microwave data (Chapter 9).

1.4.5 Macroscopic ice strength

Ice strength – at least on the macroscopic level as manifest, for example, in a uniaxial compressive strength test commonly employed in studying the mechanical properties of sea ice (Richter-Menge, 1992) – is typically defined as the peak stress, σ_{max}, sustained by a sample when a load is applied. In simplified terms, σ corresponds to the magnitude of the force, F, applied per unit area, A:

$$\sigma = \frac{F}{A} \qquad (1.38)$$

For an ideal elastic response, the strain ε resulting from a given stress σ is proportional to σ, with Young's modulus E as the proportionality constant:

$$\sigma = E\varepsilon \qquad (1.39)$$
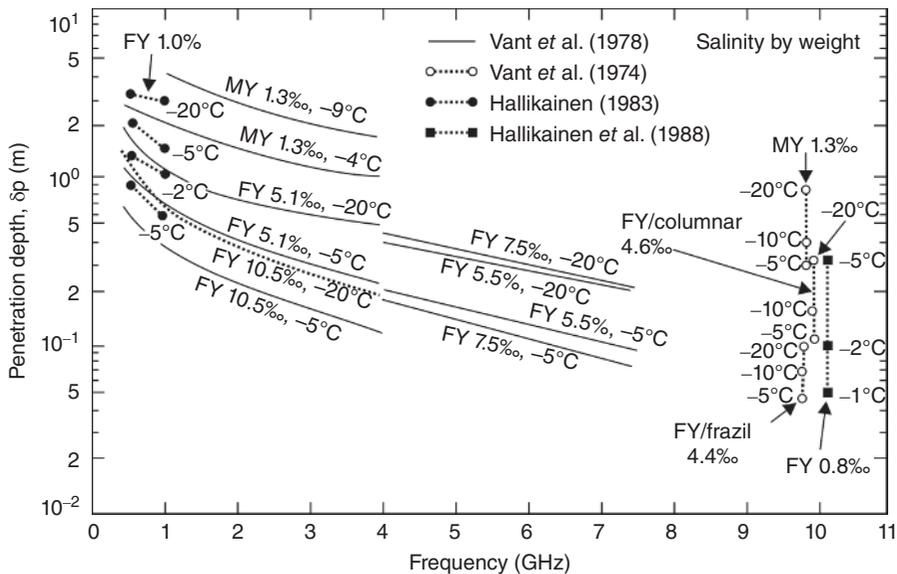
Figure 1.18 Penetration depth at microwave frequencies for different types of first-year (FY) and multi-year (MY) sea ice. Source: Hallikainen & Winebrenner, 1992. Reproduced with permission of John Wiley & Sons.

Here, strain $\varepsilon = (l - l_0)/l_0$ is defined as the relative change in linear dimension that a body experiences as it is stretched or compressed from l_0 to l. For elastic deformation, the body fully recovers from a given strain in the way an ideal spring would (Figure 1.19a). Upon reaching the yield stress σ_{max}, the sample fails catastrophically, by releasing the stored elastic energy mostly in the form of kinetic energy and sound. This process is referred to as brittle failure. The same mode of failure is experienced by a glass that shatters as it is dropped to the floor. Unlike glass, however, sea ice typically responds to a given stress not only through elastic but also through viscous (non-recoverable) deformation. For a Newtonian liquid, the latter is characterized by a linear relation between stress, σ, and strain rate, $d\varepsilon/dt$, with the viscosity of the medium η as the proportionality constant:

$$\sigma = \eta \frac{d\varepsilon}{dt} \tag{1.40}$$

Hence, deformation of natural sea ice is often best described by a material model that takes into account both elastic and viscous strain components (Mellor, 1986). Equation (1.40) implies a connection between the magnitude of the stress and the strain rate. In fact, as evident from Figure 1.19(a)–(d), the deformation of natural sea ice samples at different strain rates conforms with such a visco-elastic model, with the peak stress σ_{max} reduced by a factor of 3 as the strain rate is dropped from 10^{-2} to 10^{-5} s^{-1}. Also note that at smaller strain rates (Figure 1.19b–d), the ice exhibits ductile failure and is still capable of supporting a load after attaining σ_{max}, in contrast with the brittle failure shown in Figure 1.19(a).

It requires a highly sophisticated approach to translate these results from laboratory experiments into the real world, in which the load could be applied by a person stepping on fairly thin, young ice, with the strain rate dictated by the speed at which the foot is set down on the ice surface. Nevertheless, based on this knowledge one could devise a strategy of how to best cross a very thin, young sea ice cover if one absolutely had to. First, one would not want to apply the full load fast enough to induce catastrophic brittle failure, as this would result in the person breaking through the ice without much of a warning (i.e. prior deflection of the ice sheet; see Figure 1.19a). If strain rates were small enough to induce deformation in a ductile mode, then one

would experience the ice giving way underneath after initially appearing quite strong (at least for strain rates corresponding to the transitional brittle–ductile regime characteristic of Figure 1.19b) and, as long as the load would be reduced fast enough, the ice sheet would not fail (i.e. break).

Contrived though this example may appear, polar bears venturing out on nilas ($\leq$10 cm thick) have been observed to make intuitive use of the physics underlying such different sea ice failure modes. Thus, in ambling across the thin ice, the bear sets down each foot just long enough for the peak stress to be surpassed (at the associated strain rates in the order of a few seconds at most) and then lifts it again to place it ahead on yet unstrained ice. Indigenous hunters, such as the Iñupiat of northern Alaska, employ a similar strategy in crossing stretches of ice that would never support a person's weight if stationary for more than a few seconds at most. As the thin, warm ice flexes and is depressed below sea level, brine and seawater forced upwards through the ice onto the surface provide a visible indicator of the amount of accumulated strain.

The deformation process itself and the accommodation of strain on a microscopic level can be quite complicated. Thus, the solid ice matrix experiences deformation of atomic bonds, slip along microcracks, movement of grain boundaries and other processes (Schulson, 1999). It is the combination of all of these individual, microscopic processes that determines the macroscopic response of the ice cover. Hence, the microstructure of the ice plays an important role in determining both ice strength and mode of failure (Schulson, 1999). The contrasting properties of lake and sea ice have already been considered in Section 1.1 and similar contrasts hold for ice deformation. For typical stresses and strain rates, the response of lake ice to an imposed loading is almost exclusively elastic, with failure occurring catastrophically in a brittle mode. This gives no advance warning to anybody who is about to break through the ice, as the yield stress coincides with the complete failure of the material, similar to breaking glass. On the other hand, the lack of brine inclusions, which do not contribute to the overall strength of the material, is responsible for a somewhat higher strength of thin lake ice as compared with sea ice, which in the case of nilas can contain as much as 20% liquid-filled pores.
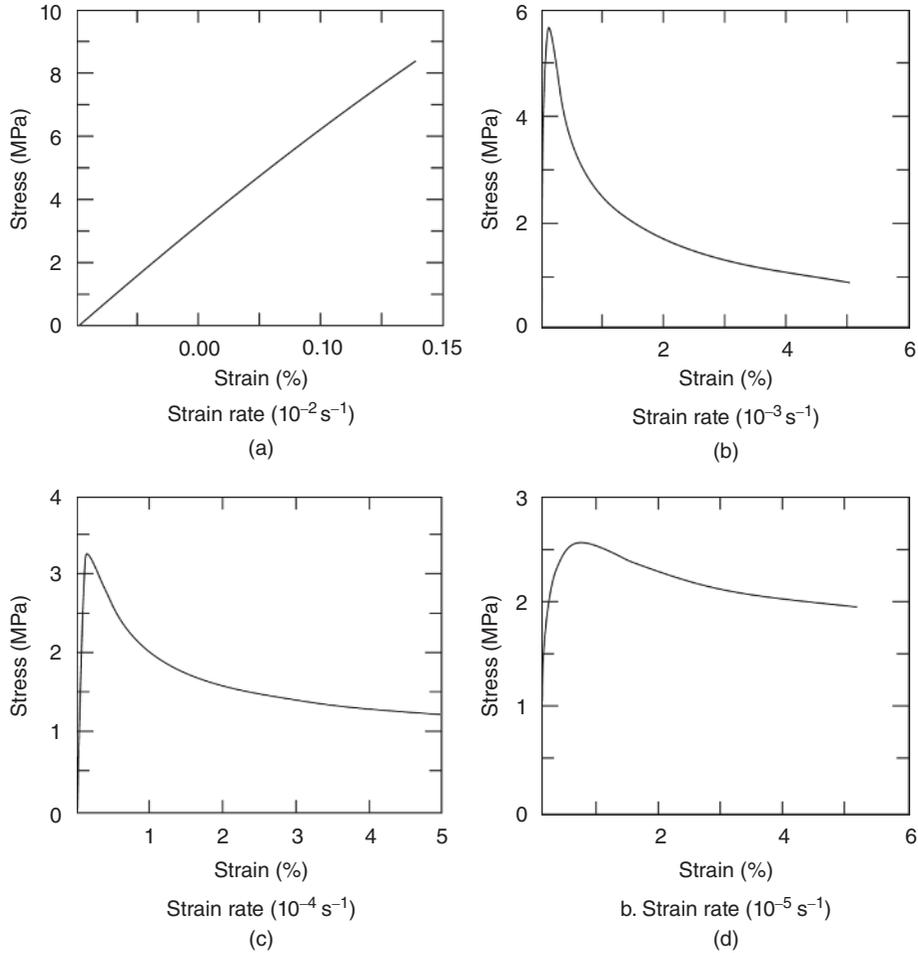
Figure 1.19 Stress–strain curves for uniaxial compression tests of granular sea ice carried out at −10°C at different strain rates. Source: Richter-Menge, 1992; see text for details.

The actual macroscopic strength (i.e. the yield stress σ_{max}; see Figure 1.19) of a sample or volume of sea ice is to a large extent controlled by the volume fraction of gas, V_a/V, and brine, V_b/V, both of which do not contribute to the mechanical strength of the material. As shown in an analysis by Assur (1960) (see summary in Weeks & Ackley, 1986) it is thus the ice cross-sectional area $(1 - \psi)$ (with ψ referred to as the 'plane porosity') that determines the magnitude of the *in situ* stress and hence the macroscopic yield stress, σ_{max}, such that:

$$\sigma_f = (1 - \psi)\sigma_0 \qquad (1.41)$$

where σ_0 would correspond to the (temperature-dependent) strength of ice with all characteristics of sea ice but zero porosity. Based on Assur's (1960) pore model (Figure 1.20), one can now derive the cross-sectional area of brine inclusions (assuming $V_a/V = 0$) in the vertical plane along which an ice sheet will typically fail under natural conditions. As shown in detail by Weeks and Ackley (1986), assuming the brine cell geometry outlined in Figure 1.20, an expression can be derived for ψ in terms of the platelet spacing, a_0, the minor and major radii of an ellipsoidal inclusion, r_a and r_b, spaced b_0 apart in the direction of the ice lamellae and a vertical separation of inclusions of length g by g_0
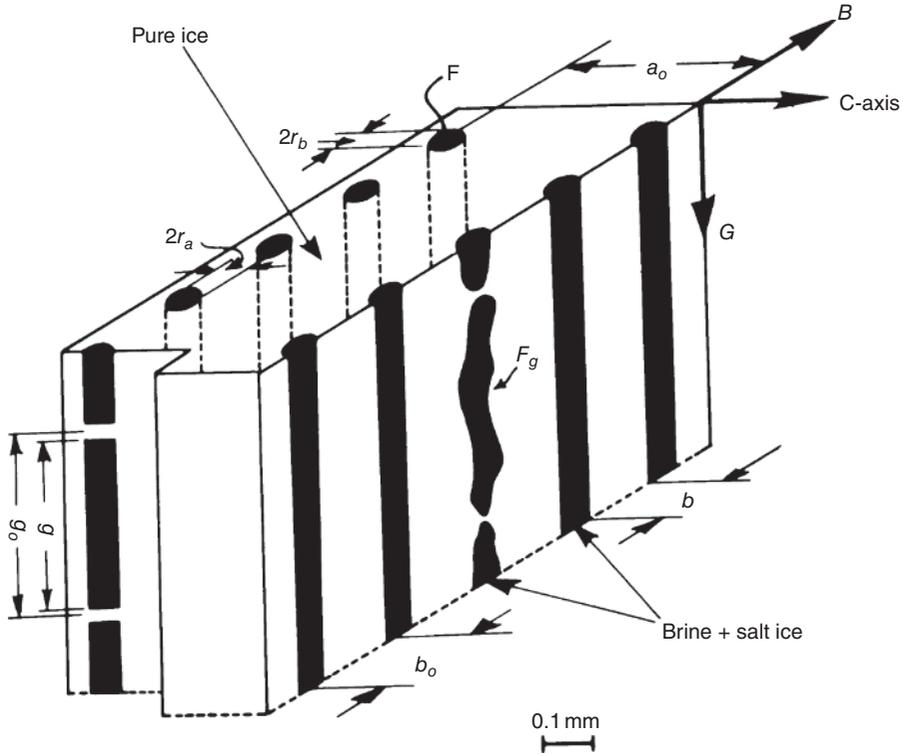
Figure 1.20 Pore microstructural model by Assur (1960).

such that equation (1.41) can be evaluated as:

$$\sigma_{\mathrm{f}} = \left(1 - 2\sqrt{\frac{r_{\mathrm{b}}}{r_{\mathrm{a}}}\frac{g}{g_0}\frac{a_0}{b_0}\frac{V_{\mathrm{b}}}{V}}\right)\sigma_0 \qquad (1.42)$$

A model of this form is difficult to evaluate in practice, as both brine volume and pore geometry depend on temperature and history of ice (in particular, melt season vs growth season). In fact, the development of the pore space is far away from trivial (Figure 1.11; Section 1.3). In addition, strength is also highly dependent on the nucleation and propagation of cracks that ultimately lead to failure. The latter depend strongly on other microstructural parameters, such as grain size or preferred alignment of crystals (Schulson, 1999). Empirical relationships are used in practice due to the significant influence of a large number of usually unknown ice properties. For example, Timco and O'Brian (1994) obtained the following equation for flexural strength of cold, growing first-year ice

$$\sigma_{\mathrm{f}} = 1.76 \ \mathrm{MPa}\,e^{-5.88\sqrt{V_b/V}} \qquad (1.43)$$

On the scale of an individual ice floe, the bending of an ice sheet results in a vertical stress/strain distribution such that maximum tensile stress is found at the top of a flexing ice sheet, with σ decreasing to zero in the interior of the ice sheet and maximum compressive stress found at a point opposite the crest in the ice. As sea ice is stronger in compression than tension by a factor of 2–4, the ice typically fails by cracks developing at the outer surface that is in tension with the crack propagating into the interior of the ice sheet. At the same time, it is the colder, less porous and hence stronger layers that determine the overall strength of an ice sheet (Figures 1.6 and 1.10). Ice strength is a property of sea ice that, probably unlike few others, is highly dependent on the scale at which it is being considered. Thus, at the scale of the ice pack, ice strength is mostly only in the order of tens to hundreds of kPa, whereas it is typically above 1 MPa in laboratory-scale experiments. The state of knowledge on the mechanical properties of sea ice has been reviewed by Timco and Weeks (2010).

1.5 Sea ice growth models, deformation and melt

1.5.1 The role of the snow cover in sea ice growth

Although it typically accounts for less than 10% of the total mass of ice in the polar seas, the snow cover plays a major role in the heat budget of sea ice. First, snow albedos are consistently higher than those of bare sea ice (Chapter 4). More importantly, snow is a good insulator, as the thermal conductivity of snow is generally lower than that of sea ice by roughly one order of magnitude (Chapter 3). The low thermal conductivity is determined by both snow texture and density. The air content is large and results in a snow density around 300 kg m^{-3}. However, most of the variability is related to the metamorphic state of the snow layer (Sturm et al., 2002). The bulk thermal conductivity of snow typically ranges between 0.1 and 0.4 W m^{-1} K^{-1}, as compared with roughly 2 W m^{-1} K^{-1} for sea ice (Massom et al., 2001; Sturm et al., 2002). Even a few centimetres of deposition on 0.5 m ice can impede ice growth by reducing the conductive heat flux, F_c (equation 1.12), by as much as 50%. As a result, thinner ice is often observed beneath snow drifts, at least on Arctic landfast ice (cf. Petrich et al., 2012c). At the same time, the sensitivity of the ice cover to changes in the oceanic heat flux increases with snow depth (equation 1.44). Another consequence of snow deposition on sea ice is a reduction in the amount of short-wave radiation entering the ice and underlying water and a temperature increase in the upper sea ice layers. Both have important ramifications for overall ice properties and the role of sea ice as a habitat for microorganisms (Chapters 13–16).

In most cases, snow-covered ice grows to be thinner than snow-free ice. However, once the load of a thicker snow cover is sufficient to depress the ice surface below the sea surface, seawater and brine may percolate either vertically or laterally through the ice cover (Maksym & Jeffries, 2000). Such seawater flooding shifts the locale of ice growth from the bottom of the ice cover to its top surface and the bottom of the snow pack. The ensuing increase in the conductive heat flux, F_c (equation 1.12), allows more ice to grow per unit area and time than would be possible through freezing at the ice bottom.

In the Arctic, snow is rarely deep enough to allow for surface flooding and snow ice formation. In the Antarctic, however, an overall thinner ice cover and higher snow accumulation rates result in widespread occurrence of this phenomenon (Maksym & Markus, 2008), with more than 50% of the surface flooded in some areas (Eicken et al., 1994; Worby et al., 1998). This has important consequences for sea ice remote sensing as it substantially changes the dielectric properties of sea ice and hence its signature in active and passive microwave remote-sensing data sets (Chapter 9). Similarly, sea ice ecology is also strongly affected by this process (Chapter 14; see infiltration layer community in Figure 1.16b).

As the flooded snow refreezes, the microstructural traces of its meteoric origin are often obliterated and it becomes exceedingly difficult to distinguish such snow ice from similarly fine-grained consolidated frazil ice. Here, the stark contrast in the stable-isotope signatures of snow, which is greatly depleted in the heavy isotopes of oxygen (^{18}O) and hydrogen (D), and ice grown from seawater with its stable, undepleted composition can help to determine the total contribution of precipitation (often referred to as meteoric ice) to the total ice thickness (Eicken et al., 1994). Numerous studies in the Southern Ocean have established that snow ice (the frozen mixture of snow and seawater and/or brine) is very common, accounting for between a few per cent to more than 50% of the total ice thickness (Maksym & Markus, 2008). The actual meteoric ice fraction is generally less than 20%. Both small- and large-scale model simulations (Fichefet & Morales Maqueda, 1999; Maksym & Jeffries, 2000; Powell et al., 2005) indicate that snow ice formation is also important on the global scale.

Snow ice formation may also help to prevent the complete removal of sea ice from areas with high oceanic heat fluxes, F_w. For example, in the eastern Weddell Sea, bottom topography and local hydrography result in winter values of F_w in excess of 100 W m^{-2} for extended periods of time (McPhee et al., 1996). In the mid-1970s this region was the site of a vast polynya that persisted for several years (Chapter 8). Considering that such high heat fluxes would halt ice growth and induce bottom melt even in midwinter, one wonders how an ice cover can survive at all in this region. Observations during the ANZFLUX study (McPhee et al., 1996) demonstrated that level ice of several tens of centimetre thickness does in fact melt at rates of several centimetres per day in the area during

intervals of high oceanic heat flux. At the surface of the ice, buffered against the oceanic heat by the ice layers below, snow ice growth seems to be able to compensate for the intermittent substantial bottom ice losses.

1.5.2 Energy budget of sea ice during growth

The fact that in the Southern Ocean, level, undeformed ice typically grows to less than 0.7 m thickness within a single year, compared with as much as 1.8 m in the Arctic, leads us to the question what exactly controls the thickness an ice floe can attain through the freezing of seawater to its underside. We will limit ourselves to the discussion of sea ice during the winter growth season in this section, a time when solar short-wave radiation is negligible.

In the case of congelation ice growth, the growth rate is determined by the energy balance at the lower boundary, i.e. the ice bottom. Here, the conductive heat flux out of the interface into the ice, F_c and the oceanic heat flux, F_w, from the underlying water into the interface are balanced by the release or uptake of latent heat, L_{si}, during freezing or melting, i.e. thickness change dH/dt (dH/d$t > 0$ during freezing):

$$- F_c + F_w + \rho_i L_{si} \frac{dH}{dt} = 0 \qquad (1.44)$$

where ρ_i is the density of ice.

The sign of a flux is a matter of convention. When considering the energy balance at one interface only, usually all fluxes are defined as either positive or negative if they are directed away from the interface; however, we consider fluxes between two interfaces and within the bulk in this section. For the sake of consistency we define fluxes as positive if heat flows upwards toward the atmosphere.

In the absence of an oceanic heat flux, the ice cover would thicken as long as heat is removed through the ice to the atmosphere. Without radiative transfer of energy into the ice, this is the case as long as the surface temperature of the ice is less than the freezing point of seawater at the lower interface. However, the ocean underlying the ice typically contains a reservoir of heat that is either remnant from solar heating of the mixed layer in summer (Maykut & McPhee, 1995) or due to transfer of heat from deeper water layers. In particular, near ice shelves, the heat flux from the ocean may be negative, giving rise to the growth of platelets at the bottom of the ice. In the

Arctic, where the amount of heat transported into the polar basin and entrained into the surface mixed layer from below the halocline is comparatively small, F_w amounts to a few W m^{-2} in most regions (Steele & Flato, 2000). In the North American Arctic, where advection of heat is minimal, the seasonal cycle of F_w is almost exclusively controlled by the absorption of solar short-wave radiation in the upper ocean, which is transferred to the ice bottom later in the season (Maykut & McPhee, 1995).

In the Southern Ocean, ocean heat flow can be in the order of several tens of W m^{-2} (Martinson & Iannuzzi, 1998). As a result, even an ice cover that is cooled substantially from the atmosphere in winter, may only grow to a maximum thickness that is determined by the balance of ocean and conductive heat flow, $F_c = F_w$. Measurements of ice thickness and surface hydrography indicate that this maximum (winter equilibrium) thickness is on the order of 0.5–0.7 m (Wadhams et al., 1987; Martinson & Iannuzzi, 1998). As shown below, such estimates can also be obtained from simple analytical modelling.

In areas where oceanic heat fluxes can episodically increase to several hundred W m^{-2} due to convective exchange with a deeper ocean well above freezing (McPhee et al., 1996), an ice cover can thin significantly, or vanish entirely, by melting from below. Such extended areas where the ocean is ice-free even in mid-winter are referred to as polynyas. The vast Weddell Sea polynya of the 1970s is the most prominent example of open water maintained through active melting and heating of the surface ocean (sensible heat polynya). Alternatively, polynyas can also form dynamically, with strong, steady winds pushing ice away from a coastline or stretches of landfast ice (latent heat polynya).

Oceanic heat and heat released from freezing is conducted to the upper surface of the ice cover and ultimately released to the atmosphere. The rate at which heat can be extracted is determined by the energy balance at the upper surface of the ice floe and snow and the ice thermal properties. For a surface at steady temperature and no solar irradiance, conservation of energy requires that the heat fluxes out of and into the surface be balanced:

$$F_L \Downarrow + F_L \Uparrow + F_s + F_e - F_c + F_m = 0 \qquad (1.45)$$

Here, the individual heat flux terms are the incoming long-wave flux, $F_L \Downarrow$; the outgoing long-wave flux,

F_L ⇑; the turbulent atmospheric sensible and latent heat fluxes F_s and F_e, respectively; the heat flux due to melting of ice at the surface, F_m (in the Arctic this is typically only relevant during the summer after the ice surface starts to melt); and the conductive heat flux from the interior of the snow or ice, F_c. Equation (1.45) is formulated with positive fluxes transporting heat upwards for consistency within this section. However, often fluxes directed away from the surface are defined as negative by convention; details on the surface energy balance can be found in Maykut (1986) and Steele and Flato (2000).

A detailed discussion of the magnitude of all these terms is given elsewhere (Maykut, 1986; Persson et al., 2002). Over Arctic multi-year ice, the net radiation balance typically does not drop below –50 W m^{-2} during winter and has its maximum in July at just over 100 W m^{-2}. The other fluxes range between a few to a few tens of W m^{-2}.

The surface and bottom heat balances are coupled through conductive heat exchange F_c with the snow and ice in between. The energy balance in sea ice is for conductive heat transfer and absorption of shortwave radiation:

$$\frac{\partial H}{\partial t} = \rho_i \, c_{si} \, \frac{\partial T}{\partial t} = \frac{\partial}{\partial z} \left(\lambda_{si} \, \frac{\partial T}{\partial z} \right) - \frac{\partial F_{sw}}{\partial z} \qquad (1.46)$$

where F_{sw} is the radiative short-wave flux (for the definition of enthalpy H see equation 1.23; the energy balance for snow is similar). In steady state ($dT/dt = 0$) and in the absence of radiative heat input ($dF_{sw}/dz = 0$), the conductive heat flux is independent of depth within sea ice and F_c is equal at both interfaces. Simplified models that couple both interfaces are discussed next.

1.5.3   Simple models of sea ice growth

A rigorous mathematical treatment of the problem of ice growth requires numerical techniques, because the individual terms in the surface energy balance (equation 1.46) depend either directly or indirectly on surface and air temperatures in a non-linear fashion and the thermal properties in equation (1.46) are temperature-dependent. Nevertheless, as demonstrated more than a century ago by Stefan (Leppäranta, 1993), through some simplifications it is actually possible to arrive at fairly accurate predictions of ice growth. Such simple, so-called degree-day models can also help us in understanding key aspects of the heat budget of sea ice and are therefore discussed in more detail below.

The principal aim of ice-growth modelling is to evaluate the growth rate, dH/dt, of sea ice as a function of time. The temperature at the ice—ocean interface is at the freezing point T_w and we assume the oceanic heat flux F_w to be known (Figure 1.21). The conductive heat flux at the bottom of the ice is largely determined by the heat flux to the atmosphere. At the interface with the atmosphere, one finds that net long-wave radiative fluxes can be described as a function of surface and air temperature during overcast. Likewise, the turbulent heat fluxes F_s and F_e depend on air and surface temperature (for a discussion of the latent heat flux F_e, see Andreas et al., 2002). As a first approximation, the net atmospheric flux can be linearized with respect to the temperature difference between air and surface, i.e. the magnitude of the net atmospheric flux F_a increases with temperature difference between surface and air:

$$F_a = -k(T_a - T_s) + F_a^0(T_a, T_s, \dots), \qquad (1.47)$$

where k is an effective heat transfer coefficient between surface and atmosphere and the residual flux F_a^0 is usually set to 0. Owing to the large ratio between latent and sensible heat stored in sea ice, sea ice grows so slowly that the ice temperature profile adjusts to the increasing ice thickness quasi-instantaneously (Carslaw & Jaeger, 1986). Hence, the temperature profile is linear in the absence of solar heating (e.g. in winter) and rapid temperature fluctuations, provided the thermal conductivity λ_{si} is homogeneous in the ice. Temperature profiles in sea ice are indeed linear during much of the growth season. This is illustrated in Figure 1.10. Considering the two-layer system of snow and ice with
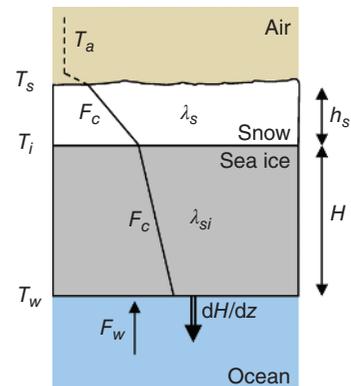

Figure 1.21 Illustration of the two-layer model of sea ice growth.

continuity in temperature and heat flux throughout snow and sea ice (Figure 1.21), Equations (1.12) and (1.47) can be written as:

$$F_a \frac{1}{k} = -(T_a - T_{as}) \tag{1.48}$$

$$F_c \frac{h_s}{\lambda_s} = -(T_{as} - T_{si}) \tag{1.49}$$

$$F_c \frac{H}{\lambda_{si}} = -(T_{si} - T_w) \tag{1.50}$$

where T_{as} and T_{si} are the interface temperatures of air and snow, and snow and ice, respectively, h_s and H are thicknesses of snow cover and sea ice, respectively, and λ_s and λ_{si} are the thermal conductivities of snow and sea ice, respectively. Realizing that $F_a = F_c$ and summing the equations, we find that the net conductive heat flux is:

$$F_a = F_c = -\frac{T_a - T_w}{\frac{1}{k} + \frac{H}{\lambda_{si}} + \frac{h_s}{\lambda_s}} \tag{1.51}$$

since $\lambda_s \approx 0.1\lambda_{si}$ we see that even a layer of snow that is thin with respect to sea ice thickness H can have a profound influence on the heat flux.

Equating (1.51) with the energy balance at the ice bottom (equation 1.44) we find:

$$\frac{dH}{dt}\rho_i L_{si} = -\frac{T_a - T_w}{\frac{1}{k} + \frac{H}{\lambda_{si}} + \frac{h_s}{\lambda_s}} - F_w \tag{1.52}$$

This equation is suitable for numerical modelling of ice thickness if time series of air temperature, snow depth and oceanic heat flux are known. However, further approximations are commonly made to allow ice thickness estimates based solely on the air temperature history: We assume the absence of an oceanic heat flux, that the atmospheric heat transfer coefficient k is constant with time and that the snow depth is proportional to the ice thickness following:

$$h_s = r_s H \tag{1.53}$$

where r_s is the constant of proportionality (note that we would expect surface flooding if r_s exceeded approx. 0.3). Integrating equation (1.52) over time we find that the ice thickness evolves according to:

$$H^2 + \frac{2\lambda_{si}}{k}\left(1 + \frac{\lambda_{si}}{\lambda_s}r_s\right)^{-1}H = \frac{2\lambda_{si}}{\rho_i L_{si}}\left(1 + \frac{\lambda_{si}}{\lambda_s}r_s\right)^{-1}\int -(T_a - T_w)dt \tag{1.54}$$

For the special case of a known and constant surface temperature, i.e. $k \Rightarrow \infty$, constant T_a and absence of snow, i.e. $r_s = 0$, equation (1.54) reduces to the solution of the Stefan problem:

$$H^2 = \frac{2\lambda_{si}(T_w - T_a)}{\rho_i L_{si}}t \tag{1.55}$$

This equation represents the most fundamental growth model of sea ice that states that the thickness of ice increases with the square root of time.

Commonly, the term:

$$\theta = \int_0^{t_e} (T_w - T_a)\,dt \tag{1.56}$$

in equation (1.54) is computed for discrete time steps $\Delta t = 1$ day; θ is then referred to as freezing degree-days, a variable easily derived from standard meteorological observations. Note that ice thickens approximately linearly with freezing degree-days if the effective heat transfer coefficient k is small and the ice is thin. Reasonable agreement with observations can often be achieved by deriving the factors in equation (1.54) empirically, typically based on ice thickness and air temperature observations at a given location. For example, Anderson (1961) found that:

$$H^2 + 5.1H = 6.7\theta \tag{1.57}$$

where H and θ are in cm and °C days, respectively.

As indicated by the quadratic nature of equation (1.54) (and equation 1.52), the thicker the ice, the lower the growth rate. As a result, differences in thickness between ice floes that started to form at different times during the winter tend to reduce with time. In the absence of ocean (or solar) heat fluxes into the ice and without any summer melt, there would be no limiting thickness for sea ice growth. However, since the oceanic heat flux, F_w, is usually >0, ice thickness has a limiting, maximum value at which conductive heat flux equals oceanic heat flux (equation 1.44) and all ice growth stops. From equations (1.52) and (1.54), this limiting or equilibrium thickness, H_{eq}, is given by:

$$H_{eq} = -\lambda_{si}\frac{T_a - T_w}{F_w}\left(1 + \frac{\lambda_{si}}{\lambda_s}r_s\right)^{-1} \tag{1.58}$$

For typical Antarctic conditions, with $T_a - T_w = -20$°C, $\lambda_{si} = 2.0$ W m^{-1} K^{-1} and $F_w = 20$ W m^{-2}, $\lambda_{si}/\lambda_i = 10$ and $r_s = 0.3$ (i.e. flooding) the limiting thickness

is 0.5 m, suggesting that the ocean does in fact limit growth of level ice. In the Arctic F_w is typically smaller by an order of magnitude and the limiting thickness greatly exceeds the amount of ice that can be grown during a single winter.

Figure 1.22 shows a comparison between the Anderson model and measurements. As evident from Figure 1.22, the impact of a snow cover on the ice thickness evolution is substantial. A simple degree-day model following equation (1.54), $H^2 + 25H = 7.3\theta$ ($r_s = 0.08$, $\lambda_{si}/\lambda_i = 6.7$, $k = 10$ W m^{-2} K^{-1}), was used to describe the development of sea ice thickness from the middle of December to June. Varying the parameter r_s, estimates were obtained for the thickness evolution without snow cover ($r_s = 0$) and with a snow cover deep enough to cause flooding ($r_s = 0.3$). Freezing degree-day models have an established place when describing ice growth and break-up but often require location-specific parameters (cf. Petrich et al., 2012a, 2014, and references therein).

Freezing degree-day models imply that ice starting to form earlier in the season will reach greater thickness by the end of the growth season than ice starting to form later in the season. However, this may not be the case if ice formation starts early in the autumn, a time typically chracterized by both high air temperatures and high precipitation (Figure 1.23a). Using a numerical model to simulate ice growth under varing temperature
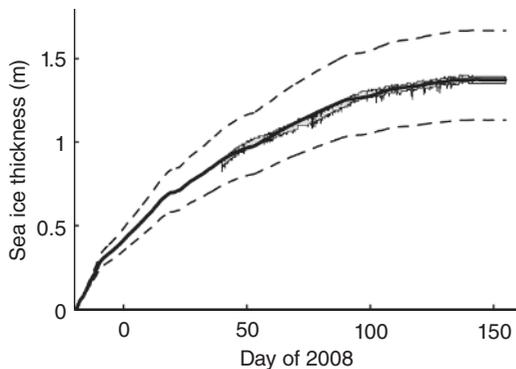
Figure 1.22 Sea ice thickness in Barrow as a function of time based on a degree-day model (thick line) and estimates of thickness development without snow and with heavy snow load (dashed lines; see text for details). Thickness measurements from an acoustic sounder are indicated by a stripe of width 4 cm from day 45 onwards. Air temperatures are based on measurements at 2 m above ground. Source: courtesy Atmospheric Radiation Measurement (ARM) Program.

and snow depth conditions, Figure 1.23(b) shows that ice forming at the end of November is expected to grow the thickest at Barrow, Alaska, by 20 May (typical end of the ice growth season). Ice starting to form in October ends up thinner. Using equation (1.5) to predict the steady-state salinity profile, Figure 1.23(b) shows that the thickness-averaged bulk salinity at the end of the growth season is lowest for the ice forming early in the season (i.e. October). As equation (1.5) is not a dynamic model we realize immediately that this finding is not the result of 'older ice having more time to desalinate'. Instead, it is due to slower growth on (a weighted) average.

1.5.4   The importance of ice deformation

Deformation of the ice cover by means of rafting and ridging (Figure 1.1) accounts for the thickest ice observed in the polar oceans and provides a mechanism for thickening even when thermodynamic growth stalls. As a result, deformation processes are particularly important in a warming climate as they may be capable of compensating for some of the thinning due to lesser ice growth and increased ice melt.

First-year pressure ridges can exhibit keels exceeding 10–20 m in depth (Strub-Klein & Sudom, 2012), presenting a particular challenge or even hazard to operations in sea ice-covered waters. When embedded in landfast sea ice and grounded, they stabilize the ice cover into the break-up season (Petrich et al., 2012a). Formation and refreezing of brash ice (ice rubble) as a result of repeat traverses of icebreaker channels in landfast ice enhances ice thickening and generally leads to the undesirable situation of ice being thicker inside the channel than next to it (Sandkvist, 1981). This practical little insight gave rise to the saying: if you break ice, you make ice.

A range of properties and processes of deformed ice differ from level ice: among these are melt-pond development, mechanical strength, ocean and atmospheric drag, and characteristics as a biological habitat. The complex interplay of different deformation processes and their overall impact on the ice thickness distribution are the topic of Chapter 2. Here it suffices to emphasize that both the thermodynamic component of ice growth and melt (potentially including brash ice) and the dynamic component of thickening through rafting or ridging contribute to the characteristics of the sea ice cover.
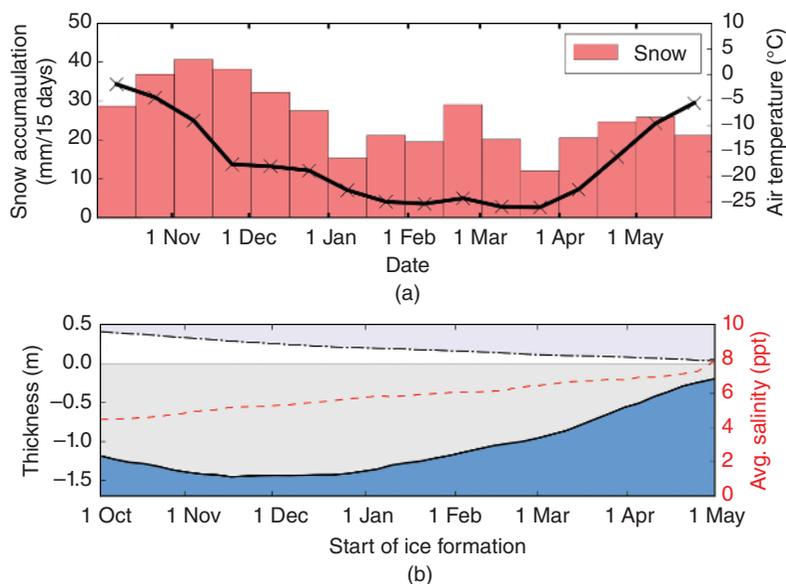
Figure 1.23 (a) Typical development of avaerage air temperature (black line) and precipitation (bars) in recent years at Barrow, Alaska. (b) Dependence of ice characteristics at the end of the growth season (20 May) on the start date of ice formation: modelled ice thickness (solid line), snow depth (dash-dotted line) and depth-averaged bulk salinity (dashed line, red). Ice forming at the end of November will reach the largest thickness at the end of the season and the later the ice starts to form, the higher the average salinity at the end of the season. Note the different scales on the x-axes. Plot (b) from Petrich et al. (2011).

1.5.5 Sea ice melt

The melt season is characterized by increasing air temperatures and irradiation. Repeat studies of the melt process of undeformed landfast first-year sea ice at Barrow, Alaska, have been performed following earlier work on the processes leading to pond evolution (Eicken et al., 2002, 2004). A recent series of studies let to detailed descriptions of the processes surrounding melt-pond evolution and sea ice decay (Petrich et al., 2012a,c; Polashenski et al., 2012). Albedo observations of these studies have been summarized and compared with multi-year ice by Perovich & Polashenski (2012). These studies highlighted that a key process (i.e. melt-pond evolution) is, to a significant extent, governed by localized positive feedbacks and spatial inhomogeneity.

Preconditioning of undeformed landfast ice for melt-pond development begins with the development of the snow cover in winter. The locations of snow drifts, once established, remain stationary in spite of episodes of winds and snowfall. On landfast ice at Barrow, the morphology of snow drifts as early as February could be directly related to melt-pond morphology and development in early June. Prior to melt, the snow drifts

were, on average, 0.1 m deeper than the average snow cover and separated by some 20 to 30 m. Following a rise in air temperature in May, the thinner patches of snow melted first, starting a positive albedo feedback loop: thin, wet snow and exposed ice are darker and absorb more light than the surrounding thicker snow patches, the ice begins to melt locally and collect melt-water. Meltwater percolating through deeper snow is occasionally observed to form superimposed ice at the ice–snow interface, fostering run-off into adjacent, ponded snow-free areas. Meltwater standing on the surface further increases the heat flux to the surface, promoting surface ablation. By the time the remaining snow has melted, a surface topography has developed, leaving the areas of originally deeper snow at a slightly higher surface elevation than the surrounding ponds. Hence, the decaying ice in these areas is interspersed with air rather than brine inclusions and easily mistaken for snow. The surface meltwater starts to drain preferentially through discrete flaws about 1 week after it first started to appear. As the water is warm, the locations of drainage widen, establishing drainage holes that can reach 10–50 cm in diameter. Surface waters

flowing towards these drainage locations contribute to enhanced local surface ablation and establish the outline of a persistent melt-pond pattern. Drainage continues for a few days until most of the surface water has drained to freeboard level. In what follows, the body of ice may either rise or fall with respect to the water level, depending on whether surface ablation or bottom ablation dominates. Ponded ice will rot considerably where particulate matter is present in the ice, locally weakening the integrity of the ice cover until it is easily broken apart by winds. Note that this description applies to undeformed sea ice with a surface that appears flat to visual inspection (except for snow drifts). In the presence of ice surface topography, the surface topography replaces snow drifts in importance (Landy et al., 2014).

A localized weakening of ice beneath melt ponds contrasts with structural weakening of an entire piece of sea ice. The latter is due to a general warming of the ice in spring, even before melt-pond formation. Petrich et al. (2012a) found that identifying the dominant mechanism is crucial to predicting local break-up; disintegration due to melt ponds is related to solar irradiance, while weakening and mechanical break-up due to swell or storms may well be predictable with freezing (or melting) degree-day models.

1.6   Conclusion

This chapter started out with an introduction to the importance of the scale of observation in the study of sea ice. Methodological innovations and advances in our understanding of sea ice as a material and a large-scale phenomenon have now opened the door to studies that are cognizant of both the vast forest and the particulars of each tree. For example, computational limitations have prevented physically realistic representations of sea ice processes in climate models. This is changing now and there is increasing interest and ability by modellers to incorporate the finer details of ice growth and ice properties into these models. Similarly, the increasing sophistication of field research methods and the realization of the importance of key sea ice processes in a global context have prompted a number of investigations that are seeking to bridge the gaps between the microscopic, macroscopic and the regional scales. Much has changed in the world of sea ice in the decade or so that passed between the publishing of the first and third editions of this book. It looks like this trend of increasing interest in the polar sea ice covers is likely to continue.

1.7   Acknowledgements

Endnotes

1 Malmgren's work and fate may also serve to illustrate how scientific investigation, exploration and the incalculable were intertwined in the early 20th century (and arguably continue to be so to some extent). Finn Malmgren's thorough and ground-breaking study of sea ice properties was prompted by Harald Sverdrup, who had suggested this work as a project to at least gain something out of the unplanned freezing in of Roald Amundsen's vessel *Maud* during the Northeast Passage expedition of 1922–25. Malmgren's experience and scientific prowess predestined him to be one of the key participants in Nobile's ill-fated airship expedition to the North Pole, where Malmgren perished in the ice pack on a trek to reach the Svalbard archipelago.

2 The data assembled by Assur originate mostly from the first half of the 20th century but have been verified to some extent by nuclear magnetic resonance studies of the liquid volume fraction (Richardson, 1976). Nevertheless, some cautions apply.

References

Anderson, D.L. (1961) Growth rate of sea ice. *Journal of Glaciology*, **3**, 1170–1172.

Andreas, E.L., Guest, P.S., Persson, P.O.G. et al. (2002), Near-surface water vapor over polar sea ice is always near ice saturation, *Journal of Geophysical Research*, **107**(C10), 8033, doi:10.1029/2000JC000411.

Arrigo, K.R., Kremer J.N. & Sullivan, C.W. (1993) A simulated Antarctic fast ice ecosystem, *Journal of Geophysical Research*, **98**(C4), 6929–6946.

Assur, A. (1960) Composition of sea ice and its tensile strength. *SIPRE Res. Rep.*, **44**.

Bennington K.O. (1967) Desalination features in natural sea ice. *Journal of Glaciology*, **49**, 845–857.

Bitz, C.M. & Lipscomb, W.H. (1999) An energy-conserving thermodynamic model of sea ice. *Journal of Geophysical Research*, **104**(C7), 15,667–15,677.

Bombosch, A. (1998) Interactions between floating ice platelets and ocean water in the southern Weddell Sea. In: *Ocean, Ice & Atmosphere: Interactions at the Antarctic continental margin* (Ed. S.S. Jacobs) *Antarctic Research Series*, **75**, 257–266.

Buckley, R.G. & Trodahl, H.J. (1987) Scattering and absorption of visible light by sea ice. *Nature*, **326**, 867–869.

Burton, J.A., R.C. Prim, and W.P. Slichter (1953). The distribution of solute in crystals grown from the melt. Pt.I. *Theoretical. Journal of Chemical Physics*, **21**, 1987–1991.

Callaghan, P.T., Dykstra R., Eccles C.D., Haskell T.G. & Seymour, J.D. (1999) A nuclear magnetic resonance study of Antarctic sea ice brine diffusivity. *Cold Regions Science and Technology*, **29**, 153–171.

Carslaw, H.S. & Jaeger, J.C. (1986) *Conduction of Heat in Solids*. Oxford University Press, Oxford.

Cottier, F., Eicken H. & Wadhams, P. (1999) Linkages between salinity and brine channel distribution in young sea ice. *Journal of Geophysical Research*, **104**(C7), 15859–15871.

Cox, G.F.N. & Weeks, W.F. (1983) Equations for determining the gas and brine volumes in sea-ice samples. *Journal of Glaciology*, **29**, 306–316.

Cox, G.F. N. & Weeks, W.F. (1986) Changes in the salinity and porosity of sea-ice samples during shipping and storage, *Journal of Glaciology*, **32**, 371–375.

Cox, G.F.N. & Weeks, W.F. (1988) Numerical simulations of the profile properties of undeformed first-year sea ice during the growth season. *Journal of Geophysical Research*, **93**, 12449–12460.

Curry, J.A., Schramm J.L. & Ebert, E.E. (1995) Sea ice-albedo climate feedback mechanism. *Journal of Climate*, **8**, 240–247.

Dieckmann, G.S., Nehrke, G., Uhlig, C. et al. (2010) Brief Communication: Ikaite ($CaCO3.6H_2O$) discovered in Arctic sea ice. *The Cryosphere*, **4**, 227–230.

Dirakev, S.N., Poyarkov S.G. & Chuvil'chikov, S.I. (2004) Laboratory modeling of small-scale convection under a growing ice cover in winter Arctic leads. *Oceanology*, **44**(1), 62–70.

Drinkwater, M.R. & Xiang, L. (2000) Seasonal to interannual variability in Antarctic sea-ice surface melt. IEEE Transact. *Geoscience and Remote Sensing*, **38**, 1827–1842.

Ehn, J.K., Mundy, C.J., Barber, D.G., Hop, H., Rossnagel, A. & Stewart, J. (2011) Impact of horizontal spreading on light propagation in melt pond covered seasonal sea ice in the Canadian Arctic. *Journal of Geophysical Research*, **116**, C00G02. doi:10.1029/2010JC006908.

Eicken, H. (1998) Factors determining microstructure, salinity and stable-isotope composition of Antarctic sea ice: deriving modes and rates of ice growth in the Weddell Sea. (Antarctic Sea Ice Physical Processes, Interactions and Variability, edited by M.O. Jeffries), *Antarctic Research Series*, **74**, 89–122.

Eicken, H. (1992a) The role of sea ice in structuring Antarctic ecosystems. *Polar Biology*, **12**, 3–13.

Eicken, H. (1992b) Salinity profiles of Antarctic sea ice: field data and model results. *Journal of Geophysical Research*, **97**, 15545–15557.

Eicken, H., Bock C., Wittig R., Miller H. & Poertner, H.-O. (2000) Nuclear magnetic resonance imaging of sea ice pore fluids: Methods and thermal evolution of pore microstructure. *Cold Regions Science and Technology*, **31**, 207–225.

Eicken, H., Grenfell T.C., Perovich D.K., Richter-Menge J.A. & Frey, K. (2004) Hydraulic controls of summer Arctic pack ice albedo. *Journal of Geophysical Research*, **109**, C08007, doi:101029/2003JC001989.

Eicken, H., Krouse H.R., Kadko D. & Perovich, D.K. (2002) Tracer studies of pathways and rates of meltwater transport through Arctic summer sea ice. *Journal of Geophysical Research*, **107**, 10.1029/2000JC000583.

Eicken, H., Lange M.A., Hubberten H.-W. & Wadhams, P. (1994) Characteristics and distribution patterns of snow and meteoric in the Weddell Sea and their contribution to the mass balance of sea ice. *Annals of Geophysics*, **12**, 80–93.

Eide, L.I. & Martin, S. (1975) The formation of brine drainage features in young sea ice. *Journal of Glaciology*, **14**(7), 137–154.

Feltham, D.L., Worster M.G. & Wettlaufer, J.S. (2002) The influence of ocean flow on newly forming sea ice. *Journal of Geophysical Research*, **107**(C2), 3009, doi:10.1029/2000JC000559.

Fichefet, T. & Morales Maqueda, M.A. (1999) Modelling the influence of snow accumulation and snow-ice formation on the seasonal cycle of the Antarctic sea-ice cover. *Climate Dynamics*, **15**, 251–268.

Fletcher, N.H. (1970) *The Chemical Physics of Ice*. Cambridge University Press, Cambridge.

Flocco, D., Schroeder D., Feltham D.L. & Hunke, E.C. (2012) Impact of melt ponds on Arctic sea ice simulations from 1990 to 2007. *Journal of Geophysical Research*, **117**, C09032, doi:10.1029/2012JC008195.

Freitag, J. (1999) The hydraulic properties of Arctic sea ice – implications for the small-scale particle transport (in German). *Berichte zur Polarforschung*, **325**, 1–150.

Freitag, J. & Eicken, H. (2003) Meltwater circulation and permeability of Arctic summer sea ice derived from hydrological field experiments. *Journal of Glaciology*, **49**, 349–358.

Golden, K.M., Ackley, S.F. & Lytle, V.I. (1998) The percolation phase transition in sea ice. *Science*, **282**, 2238–2241.

Golden, K.M., Eicken, H., Heaton, A.L., Miner, J., Pringle, D.J. & Zhu, J. (2007) Thermal evolution of permeability and microstructure in sea ice. *Geophysical Research Letters*, **34**, L16501, doi:10.1029/2007GL030447.

Gough, A.J., Mahoney, A.R., Langhorne, P.J., Williams, M.J. M. & Haskell, T.G. (2012) Sea ice salinity and structure: A winter time series of salinity and its distribution. *Journal of Geophysical Research*, **117**, C03008, doi:10.1029/2011JC007527.

Griewank, P.J. & Notz, D. (2013) Insights into brine dynamics and sea ice desalination from a 1-D model study of gravity drainage. *Journal of Geophysical Research Oceans*, **118**, 3370–3386.

Hallikainen, M. & Winebrenner, D.P. (1992) The physical basis for sea ice remote sensing. In: *Microwave Remote Sensing of Sea Ice* (Ed. by F.D. Carsey), pp. 29–46. Geophysical Monograph 68. American Geophysical Union, Washington.

Hobbs, P.V. (1974) *Ice Physics*. Clarendon Press, Oxford.

Hu, Y., Wolf-Gladrow D.A., Dieckmann G.S., Völker C. & Nehrke, G. (2014) A laboratory study of ikaite (CaCO3·6H2O) precipitation as a function of pH, salinity, temperature and phosphate concentration. *Marine Chemistry*, **162**, 10–18.

Hunke, E.C., D. Notz, A.K. Turner, and M. Vancoppenolle (2011). The multiphase physics of sea ice: a review for model developers. *The Cryosphere*, **5**, 989–1009, doi:10.5194/tc-5-989-2011

IOC, SCOR and IAPSO (2010) The international thermodynamic equation of seawater–2010 In: *Calculation and Use of Thermodynamic Properties*. Intergovernmental Oceanographic Commission, Manuals and Guides No. 56. UNESCO (English).

Jeffries, M.O., Shaw R.A., Morris K., Veazey A.L. & Krouse, H.R. (1994) Crystal structure, stable isotopes (d18O) and development of sea ice in the Ross, Amundsen & Bellingshausen seas, Antarctica. *Journal of Geophysical Research*, **99**, 985–995.

Jeffries, M.O., Weeks W.F., Shaw R. & Morris, K. (1993) Structural characteristics of congelation and platelet ice and their role in the development of Antarctic land-fast sea ice, *Journal of Glaciology*, **39**, 223–238.

Katlein, C., Nicolaus, M. & Petrich, C. (2014) The anisotropic scattering coefficient of sea ice. *Journal of Geophysical Research Oceans*, **119**, doi:10.1002/2013JC009502.

Kovacs, A. (1996) Sea ice: Part I. Bulk salinity versus ice floe thickness. *CRREL Report* 96–7.

Krembs, C., Eicken, H. & Deming, J.W. (2011) Exopolymer alteration of physical properties of sea ice and implications for ice habitability and biogeochemistry in a warmer Arctic. *Proceedings of the National Academy of Sciences USA*, **108**, 3653–3658. doi: 10.1073/pnas.1100701108.

Lake, R.A. & Lewis, E.L. (1970) Salt rejection by sea ice during growth. *Journal of Geophysical Research*, **75**, 583–597.

Landy, J., Ehn J., Shields M. & Barber, D. (2014) Surface and melt pond evolution on landfast first-year sea ice in the Canadian Arctic Archipelago. *Journal of Geophysical Research Oceans*, **119**(5), 3054–3075.

Lange, M.A., Ackley S.F., Wadhams P., Dieckmann G.S. & Eicken, H. (1989) Development of sea ice in the Weddell Sea, Antarctica. *Annals of Glaciology*, **12**, 92–96.

Langhorne, P.J. & Robinson, W.H. (1986) Alignment of crystals in sea ice due to fluid motion. *Cold Regions Science and Technology*, **12**(2), 197–215.

Leonard, G.H., Purdie C.R., Langhorne P.J., Haskell T.G., Williams M.J.M. & Frew, R.D. (2006) Observations of platelet ice growth and oceanographic conditions during the winter of 2003 in McMurdo Sound, Antarctica. *Journal of Geophysical Research*, **111**, C04012. doi:10.1029/2005JC002952

Leppäranta, M. (1993) A review of analytical models of sea-ice growth. *Atmosphere-Ocean*, **31**, 123–138.

Leppäranta, M. & Manninen, T. (1988) The brine and gas content of sea ice with attention to low salinities and high temperatures. *Finnish Institure for Marine Research Internal Report*, 88–82, Helsinki.

Light B., Maykut G.A. & Grenfell, T.C. (2003) Effects of temperature on the microstructure of first-year Arctic sea ice, *Journal of Geophysical Research*, **108**(C2), 3051, doi:10.1029/2001JC000887.

Lin, F.C., Kong J.A., Shin R.T., Gow A.J. & Arcone S.A. (1988) Correlation function study for sea ice. *Journal of Geophysical Research*, **93**, 14055–14063.

Maksym, T. & Markus, T. (2008) Antarctic sea ice thickness and snow-to-ice conversion from atmospheric reanalysis and passive microwave snow depth. *Journal of Geophysical Research*, **113**, C02S12, doi:10.1029/2006JC004085.

Maksym, T. & Jeffries, M.O. (2000) A one-dimensional percolation model of flooding and snow ice formation on Antarctic sea ice. *Journal of Geophysical Research*, **105**, 26313–26331.

Malmgren, F. (1927) On the properties of sea-ice. *Norwegian North Polar Expedition "Maud"* 1918–1925, **1**, 1–67.

Marion, G.M. & Kargel, J.S. (2008) *Cold Aqueous Planetary Geochemistry with FREZCHEM: From Modeling to the Search for Life at the Limits*. Springer, Berlin.

Marion, G.M. & Grant, S.A. (1997) Physical chemistry of geochemical solutions at subzero temperatures. *CRREL Special Report*, **97–10**, 349–356.

Martinson, D.G. & Iannuzzi, R.A. (1998) Antarctic ocean-ice interaction: Implications from ocean bulk property distributions in the Weddell Gyre. In: *Antarctic Sea Ice: Physical Processes, Interactions and Variability* (Ed. by M.O. Jeffries). American Geophysical Union, Washington. Antarctic Research Series, **74**, 243–271.

Massom, R.A. et al. (2001) Snow on Antarctic sea ice. *Review of Geophysics*, **39**, 413–445.

Maus, S. & De la Rosa, S. (2012) Salinity and solid fraction of frazil and grease ice. *Journal of Glaciology*, **58**, doi:10.3189/2012JoG11J110.

Maykut, G.A. (1986) The surface heat and mass balance. In: *The Geophysics of Sea Ice*. (Ed. by N. Untersteiner), pp. 395–463. Martinus Nijhoff Publ., Dordrecht (NATO ASI B146).

Maykut, G.A. & McPhee, M.G. (1995) Solar heating of the Arctic mixed layer. *Journal of Geophysical Research*, **100**, 24691–24703.

McPhee, M.G., Ackley, S.F., Guest, P. et al. (1996) The Antarctic Zone Flux Experiment. *Bulletin of the American Meteorological Society*, **77**, 1221–1232.

McPhee, M.G., Stanton, T.P., Morison, J.H. & Martinson, D.G. (1998) Freshening of the upper ocean in the central Arctic:

Is perennial sea ice disappearing? *Geophysical Research Letters*, **25**, 1729–1732.

Mellor, M. (1986) Mechanical behavior of sea ice. In: *The Geophysics of Sea Ice*. (Ed. by N. Untersteiner), pp. 165–281. Martinus Nijhoff Publ., Dordrecht (NATO ASI B146).

Millero, F.J., Feistel, R., Wright, D.G. & McDougall, T.J. (2008) The composition of standard seawater and the definition of the reference-composition salinity scale. *Deep-Sea Research Part 1*, 55, 50–72.

Nakawo, M. & Sinha, N.K. (1981) Growth rate and salinity profile of first-year sea ice in the high Arctic. *Journal of Glaciology*, **27**, 315–330.

Nakawo, M. & Sinha, N.K. (1984) A note on brine layer spacing of first-year sea ice. *Atmosphere-Ocean*, **22**, 193–206.

Naumann, A.K., Notz, D., Håvik, L. & Sirevaag, A. (2012) Laboratory study of initial sea-ice growth: properties of grease ice and nilas. *The Cryosphere*, **6**, 729–741.

Niedrauer, T.M. & Martin, S. (1979) An experimental study of brine drainage and convection in young sea ice. *Journal of Geophysical Research*, **84**, 1176–1186.

Nield, D.A. & Bejan, A. (1998) *Convection in Porous Media*. Springer-Verlag, NY, USA.

Notz, D., McPhee, M.G., Worster, M.G., Maykut, G.A., Schlünzen, K.H. & Eicken, H. (2003) Impact of underwater-ice evolution on Arctic summer sea ice. *Journal of Geophysical Research*, **108**(C7), 3223, doi:10.1029/2001JC00173.

Notz, D. & Worster, M.G. (2009) Desalination processes of sea ice revisited. *Journal of Geophysical Research*, **114**, C05006, 1–10. doi:10.1029/2008JC004885.

Ono, N. (1967) Specific heat and heat of fusion of sea ice. In: *Physics of Snow and Ice*. (Ed.H. Onura), vol. **1**, 599–610.

Ono, N. (1968) Thermal properties of sea ice: IV, thermal constants of sea ice (in Japanese). *Low Temperature Science Series A*, **26**, 329–349.

Papadimitriou, S., Kennedy, H., Kennedy, D.P. & Thomas, D.N. (2013) Ikaite solubility in seawater-derived brines at 1 atm and sub-zero temperatures to 265 K. *Geochimica et Cosmochimica Acta*, **109**, 241–253

Papadimitriou, S., Kennedy, H., Kennedy, D.P. & Thomas, D.N. (2014) Kinetics of ikaite precipitation and dissolution in seawater-derived brines at sub-zero temperatures to 265 K. *Geochimica et Cosmochimica Acta*, **140**, 199–211.

Perovich, D.K. (1998) Optical properties of sea ice. In: *Physics of ice-covered seas*, vol. **1**. (Ed. by M. Leppäranta), pp. 195–230, University of Helsinki, Helsinki.

Perovich D.K., Grenfell T.C., Richter-Menge J.A., Light B., Tucker III, W.B. & Eicken H. (2003) Thin and thinner: Sea ice mass balance measurements during SHEBA, *Journal of Geophysical Research*, **108**(C3), 8050, doi:10.1029/2001JC001079.

Perovich, D.K. & Gow, A.J. (1996) A quantitative description of sea ice inclusions. *Journal of Geophysical Research*, **101**(C8), 18,327–18,343.

Perovich, D.K., Light, B., Eicken, H., Jones, K.F., Runciman, K. & Nghiem, S.V. (2007) Increasing solar heating of the Arctic Ocean and adjacent seas, 1979–2005: Attribution and role in the ice-albedo feedback, *Geophysical Research Letters*, **34**, L19505, doi:19510.11029/12007/GL031480.

Persson, P.O. G., Fairall C.W., Andreas E.L., Guest P.S. & Perovich, D.K. (2002) Measurements near the Atmospheric surface flux group tower at SHEBA: Near-surface conditions and surface energy budget. *Journal of Geophysical Research*, **107**, doi:10.1029/2000JC000705.

Petrich, C., Langhorne P.J. & Sun, Z.F. (2006) Modelling the interrelationships between permeability, effective porosity and total porosity in sea ice. *Cold Regions Science and Technology*, **44**, 131–144.

Petrich, C., Langhorne P.J. & Haskell, T.G. (2007) Formation and structure of refrozen cracks in land-fast first-year sea ice, *Journal of Geophysical Research*, **112**, C04006, doi:10.1029/2006JC003466.

Petrich, C., Langhorne, P.J. & Eicken, H. (2011) Modelled bulk salinity of growing first-year sea ice and implications for ice properties in spring. In: *Proceedings of the 21st International Conference on Port and Ocean Engineering under Arctic Conditions (POAC), Montreal, Quebec, Canada, 10–14 July 2011*. Paper POAC11–187, 10 pp.

Petrich, C., Eicken, H., Zhang, J., Krieger, J.R., Fukamachi, Y. & Ohshima, K.I. (2012a) Coastal sea ice melt and break-up in northern Alaska: processes and possibility to forecast, *Journal of Geophysical Research*, **117**, C02003, 1–19

Petrich, C., Nicolaus, M. & Gradinger, R. (2012b) Sensitivity of the light field under sea ice to spatially inhomogeneous optical properties and incident light assessed with three-dimensional Monte Carlo radiative transfer simulations. *Cold Regions Science and Technology*, **73**, 1–11.

Petrich, C., Eicken, H., Polashenski, C.M. et al. (2012c) Snow dunes: a controlling factor of melt pond distribution on Arctic sea ice. *Journal of Geophysical Research*, **117**, C09029, 1–10, doi:10.1029/2012JC008192.

Petrich, C., Karlsson, J. & Eicken, H. (2013) Porosity of growing sea ice and potential for oil entrainment. *Cold Regions Science and Technology*, **87**, 27–32.

Petrich, C., Tivy, A.C. & Ward, D.H. (2014) Reconstruction of historic sea ice conditions in a sub-Arctic lagoon. *Cold Regions Science and Technology*, **98**, 55–62.

Polashenski, C., Perovich, D. & Courville, Z. (2012) The mechanisms of sea ice melt pond formation and evolution. *Journal of Geophysical Research*, **117**, C01001, 1–23. doi:10.1029/2011JC007231.

Powell, D.C., Markus, & T., Stössel, A. (2005) Effects of snow depth forcing on Southern Ocean sea ice simulations, *Journal of Geophysical Research*, **110**, C06001, doi:10.1029/2003JC002212.

Pringle, D.J., Eicken H., Trodahl H.J. & Backstrom, L.G.E. (2007) Thermal conductivity of landfast Antarctic and Arctic sea ice. *Journal of Geophysical Research*, **112**, C04017, doi:10.1029/2006JC003641.

Pringle, D.J., Miner J.E., Eicken H. & Golden, K.M. (2009) Pore-space percolation in sea ice single cystals. *Journal of Geophysical Research*, **114**, C12, doi:10.1029/2008JC005145

Rees Jones, D.W. & Worster, M.G. (2013) A simple dynamical model for gravity drainage from growing sea ice. *Geophysical Research Letters*, **40**, 307–311. doi:10.1029/2012GL054301.

Reimnitz, E., Kempema E.W., Weber W.S., Clayton J.R. & Payne, J.R. (1990) Suspended-matter scavenging by rising frazil ice. *CRREL Monographs*, **90–1**, 97–100.

Richter-Menge, J.A. (1992) Compressive strength of frazil sea ice. *Proceedings IAHR Symposium on Ice, Banff, Alberta*, **2**, 1065–1074.

Rothrock, D.A., Yu Y. & Maykut, G.A. (1999) Thinning of the Arctic sea-ice cover. *Geophysical Research Letters*, **26**, 3469–3472.

Sandkvist, J. (1981) Conditions in brash ice covered channels with repeated passages. In: *Proceedings of the 6th International Conference on Port and Ocean Engineering under Arctic Conditions (POAC), Québec City, Canada, 27–31 July 1981*, pp. 244–252.

Schanda, E. (1986) *Physical Fundamentals of Remote Sensing*. Springer-Verlag, Berlin.

Schulson E.M. (1999) The structure and mechanical behavior of ice. *JOM*, **51**, 21–27.

Schwerdtfeger, P. (1963) The thermal properties of sea ice. *Journal of Glaciology*, **4**, 789–807.

Smedsrud, L.H. (2001) Frazil-ice entrainment of sediment: large-tank laboratory experiments. *Journal of Glaciology*, **47**, 461–471.

Smith, R.E.H., Harrison W.G., Harris L.R. & Herman A.W. (1990) Vertical fine structure of particulate matter and nutrients in sea ice of the high Arctic. *Canadian Journal of Fisheries and Aquatic Science*, **47**, 1348–1355.

Steele, M. & Flato, G.M. (2000) Sea ice growth, melt and modeling: a survey. In: *The Freshwater Budget of the Arctic Ocean* (Ed. by E.L. Lewis), pp. 549–587. Kluwer Academic Publishers, Dordrecht.

Stogryn, A. (1987) An analysis of the tensor dielectric constant of sea ice at microwave frequencies. IEEE Transact. *Geoscience and Remote Sensing*, **GE-25**, 147–158.

Strub-Klein, L. & Sudom, D. (2012) A comprehensive analysis of the morphology of first-year sea ice ridges. *Cold Regions Science and Technology*, **82**, 94–109.

Sturm, M., Perovich, D.K. & Holmgren J. (2002) Thermal conductivity and heat transfer through the snow on the ice of the Beaufort Sea. *Journal of Geophysical Research*, **107**, doi:10.1029/2000JC000409.

Timco, G.W. & O'Brian, S. (1994) Flexural strength equation for sea ice. *Cold Regions Science and Technology*, **22**(3), 285–298.

Timco, G.W. & Weeks, W.F. (2010) A review of the engineering properties of sea ice. *Cold Regions Science and Technology*, **60**, 107–129.

Tyshko, K.P., Fedotov V.I. & Cherepanov, I.V. (1997) Spatio-temporal variability of the Arctic seas' ice cover structure. In: *Sea ice* (Eds. I.E. Frolov & V.P. Gavrilo), pp. 191–213. Gidrometeoizdat, St. Petersburg.

UNESCO (1978) *Eighth Report of the Joint Panel On Oceanographic Tables and Standards Unesco Technical Papers in Marine Science, 28*. Unesco, Paris.

Untersteiner, N. (1961) On the mass and heat budget of Arctic sea ice. *Archives for Meteorology, Geophysics and Bioclimatology Series A*, **12**, 151–182.

Untersteiner, N. (1968) Natural desalination and equilibrium salinity profile of perennial sea ice. *Journal of Geophysical Research*, **73**, 1251–1257.

Vancoppenolle, M., Fichefet, T. & Goosse, H. (2009) Simulating the mass balance and salinity of Arctic and Antarctic sea ice. 2. Importance of sea ice salinity variations. *Ocean Modelling*, **27**, 54–69.

Wakatsuchi, M. (1983) Brine exclusion process from growing sea ice. *Low Temperature Science*, **A33**, 29–65.

Wakatsuchi, M. & Ono, N. (1983) Measurements of salinity and volume of brine excluded from growing sea ice. *Journal of Geophysical Research*, **88**(C5), 2943–2951.

Wadhams, P., Lange, M.A. & Ackley, S.F. (1987) The ice thickness distribution across the Atlantic sector of the Antarctic Ocean in midwinter. *Journal of Geophysical Research*, **92**, 14535–14552.

Weeks, W.F. (2010) *On Sea Ice*. University of Alaska Press, Fairbanks, AK, USA.

Weeks, W.F. & Ackley, S.F. (1986) The growth, structure and properties of sea ice. In: *The Geophysics of Sea Ice*. (Ed. N. Untersteiner), pp. 9–164. Plenum Press, New York (NATO ASI B146).

Weeks, W.F. & Lee, O.S. (1962) The salinity distribution in young sea-ice. *Arctic*, **15**, 92–108.

Weeks, W.F. & Wettlaufer, J.S. (1996) Crystal orientations in floating ice sheets. In: *The Johannes Weertman Symposium*. (Eds. R.J. Arsenault et al.), pp. 337–350. The Minerals, Metals and Materials Society, Warrendale, PA.

Wettlaufer, J.S., Worster, M.G. & Huppert, H.E. (1997) Natural convection during solidification of an alloy from above with application to the evolution of sea ice. *Journal of Fluid Mechanics*, **344**, 291–316.

Worby, A.P., Massom, R.A., Allison, I., Lytle, V.I. & Heil, P. (1998) East Antarctic sea ice: a review of its structure, properties and drift. In: *Antarctic Sea Ice Physical Processes, Interactions and Variability* (Ed. M.O. Jeffries). American Geophysical Union, Washington. Antarctic Research Series, **74**, 41–67.

Worster, M.G. & Wettlaufer, J.S. (1997) Natural convection, solute trapping & channel formation during solidification of saltwater. *Journal of Physical Chemistry B*, **101**, 6132–6136.

Yen, Y.C., Cheng, K.C. & Fukusako, S. (1991) Review of intrinsic thermophysical properties of snow, ice, sea ice & frost. In: *Proceedings 3rd International Symposium on Cold Regions Heat Transfer, Fairbanks, AK, June 11–14, 1991*. (Eds. J.P. Zarling & S.L. Faussett), pp. 187–218. University of Alaska, Fairbanks.

Zotikov, I.A., Zagorodnov, V.S. & Raikovsky, J.V. (1980) Core drilling through the Ross Ice Shelf (Antarctica) confirmed basal freezing. *Science*, **207**, 1463–1465.